

Benchmarking boron carbide equation of state using computation and experiment

Shuai Zhang,^{1,2,*} Michelle C. Marshall,^{1,†} Lin H. Yang,¹ Philip A. Sterne,¹ Burkhard Militzer,^{3,4,‡} Markus Däne,¹ James A. Gaffney,¹ Andrew Shamp,¹ Tadashi Ogitsu,¹ Kyle Caspersen,¹ Amy E. Lazicki,¹ David Erskine,¹ Richard A. London,¹ Peter M. Celliers,¹ Joseph Nilsen,¹ and Heather D. Whitley^{1,§}

¹*Lawrence Livermore National Laboratory, Livermore, California 94550, USA*

²*Laboratory for Laser Energetics, University of Rochester, Rochester, New York 14623, USA*

³*Department of Earth and Planetary Science, University of California, Berkeley, California 94720, USA*

⁴*Department of Astronomy, University of California, Berkeley, California 94720, USA*

(Dated: October 26, 2021)

Boron carbide (B_4C) is of both fundamental scientific and practical interest due to its structural complexity and how it changes upon compression, as well as its many industrial uses and potential for use in inertial confinement fusion (ICF) and high energy density physics experiments. We report the results of a comprehensive computational study of the equation of state (EOS) of B_4C in the liquid, warm dense matter, and plasma phases. Our calculations are cross-validated by comparisons with Hugoniot measurements up to 61 megabar from planar shock experiments performed at the National Ignition Facility (NIF). Our computational methods include path integral Monte Carlo, activity expansion, as well as all-electron Green's function Korringa-Kohn-Rostoker and molecular dynamics that are both based on density functional theory. We calculate the pressure-internal energy EOS of B_4C over a broad range of temperatures ($\sim 6 \times 10^3$ – 5×10^8 K) and densities (0.025 – 50 g/cm³). We assess that the largest discrepancies between theoretical predictions are $\lesssim 5\%$ near the compression maximum at 1 – 2×10^6 K. This is the warm-dense state in which the K shell significantly ionizes and has posed grand challenges to theory and experiment. By comparing with different EOS models, we find a Purgatorio model (LEOS 2122) that agrees with our calculations. The maximum discrepancies in pressure between our first-principles predictions and LEOS 2122 are $\sim 18\%$ and occur at temperatures between 6×10^3 – 2×10^5 K, which we believe originate from differences in the ion thermal term and the cold curve that are modeled in LEOS 2122 in comparison with our first-principles calculations. In order to account for potential differences in the ion thermal term, we have developed three new equation of state models that are consistent with theoretical calculations and experiment. We apply these new models to 1D hydrodynamic simulations of a polar direct-drive NIF implosion, demonstrating that these new models are now available for future ICF design studies. (LLNL-JRNL-812984)

I. INTRODUCTION

The design of high energy density and inertial confinement fusion experiments requires a good description of the ablator equation of state (EOS). Materials that are typically used as ablators are plastics, such as hydrocarbons (CH) and glow discharge polymers (GDP).^{1–4} However, formation of condensed phase microstructures and mixing with the DT fuel during implosion could affect the performance of the ignition target.^{5,6} Additional materials with higher density and hardness, such as high-density carbon (HDC), boron-materials, and beryllium also provide current and future options for ablators.^{7–11} In comparison to plastics, these high-tensile strength materials typically exhibit ablation pressures that are 15–20% higher.⁷ Using these materials as the ablator can have higher x-ray absorption and use a shorter laser pulse with a higher ablation rate for a given temperature, and thereby require a thinner ablator shell while maintaining the same mass and outer diameter.^{7,10,12} Ablators doped with boron have also been the subject of more recent proposals to use reactions with γ -rays as a means of quantifying ablator mix in inertial confinement fusion (ICF) experiments,¹³ and boron carbide is of particular interest for ignition experiments because a method for producing

hollow capsules has already been demonstrated.¹⁴

In recent studies, Zhang *et al.* combined several computational methods to set accurate constraint for the EOS of boron (B)¹² and boron nitride (BN)¹⁵ over a wide range of temperatures (~ 0.2 eV–50 keV) and densities (0.1–20 times compression). They also conducted laser shock experiments at the Omega laser facility and the National Ignition Facility (NIF) to measure the Hugoniot EOS to pressures of 10–60 megabar (Mbar) and demonstrated remarkable agreement with the first-principles predictions. Their data have enabled building new EOS tables (X52 for B and X2152 for BN) based on the quotidian EOS (QEOS) model^{16,17} and clarifying the dominating physics (cold curve, ion thermal, or electron thermal) at different regions of the temperature-density space. They also performed 1D hydrodynamic simulations of polar direct-drive exploding-pusher experiments¹⁸ to explore the performance sensitivity to the EOS.

Boron carbide is another important member in the family of boron materials. At ambient condition, it has a high melting point, superior hardness, low specific weight, good resistance to chemical agents, and high neutron absorption cross section. These outstanding properties allow it to be widely used for mechanical, electrical, chemical, and nuclear applications.¹⁹ The ambient crystal structure of B_4C has rhombohedral symmetry (space

group R $\bar{3}m$), similar to that of α -B, and is characterized by B-rich icosahedra and C-rich chains. X-ray diffraction experiments reveal this structure to be stable under static compression at up to 126 GPa.²⁰ Single-crystal experiments show that the icosahedral units are less compressible than the unit cell volume and the static compression is governed by force transfer between the rigid icosahedra.²¹ However, dramatic structural changes have been reported under shock compression^{22–24}, scratching and nanoindentation^{25–27}, or depressurization²⁸ and attributed to amorphization or structural transition that is accompanied by changes in hardness, compressibility, or elastic modulus.^{22,29,30} There have also been studies that show the shear strength of boron-rich boron carbide can be lowered due to nanotwins³¹ and multi-scale molecular dynamics (MD) simulations that relate structural changes to hydrostaticity of compression³².

Over the last few years, knowledge about the EOS of boron carbide has advanced significantly. The EOS and melting curve of B₄C were constructed by Molodets *et al.*³³ that agree with available experiments at up to megabar pressures, featuring melting with a negative Clapeyron slope at pressures below 150 GPa and a positive one above 170 GPa. Jay *et al.*³⁴ performed comprehensive *ab initio* calculations for boron carbide at up to 80 GPa and 2000 K, and their temperature-pressure-concentration phase diagrams show phase separation of boron carbides in multiple stages and into B and C at above 70 GPa. Fratanduono *et al.*³⁵ extended the Hugoniot, sound velocities, and thermodynamic properties measurements of liquid B₄C to 700 GPa. Shamp *et al.*³⁶ performed MD calculations based on density functional theory (DFT) to determine the Hugoniot curve up to 1500 GPa, and predicted discontinuities along the Hugoniot at <100 GPa as results of phase separation and transformation in solid B₄C. An equation of state table (LEOS 2122) based on an average atom-in-jellium model (Purgatorio)³⁷ has thus been developed that fits all available experimental Hugoniot data above 100 GPa³⁵. However, accurate EOS at higher pressures and temperatures, in particular those corresponding to the partially ionized, warm dense state, is still unknown.

The goal of this work is to benchmark the EOS of B₄C in a wide range of temperatures and pressures by combining theoretical calculations and experiments. Our theoretical methods include path integral Monte Carlo (PIMC), pseudopotential DFT-MD approaches realized in multiple schemes, an activity expansion method (ACTEX), and an all-electron, Green’s function Korringa-Kohn-Rostoker (KKR) method. Our experiments consist of seven Hugoniot measurements conducted at the NIF. The paper is organized as follows: Sec. II outlines our computational details; Sec. III describes our shock experiments; Sec. IV compares our EOS and Hugoniot results from computation and experiments, constructs new EOS models, and explores the role of EOS in hydrodynamic simulations; Sec. V discusses the microscopic physics of B₄C by combining electronic structure and QEOS per-

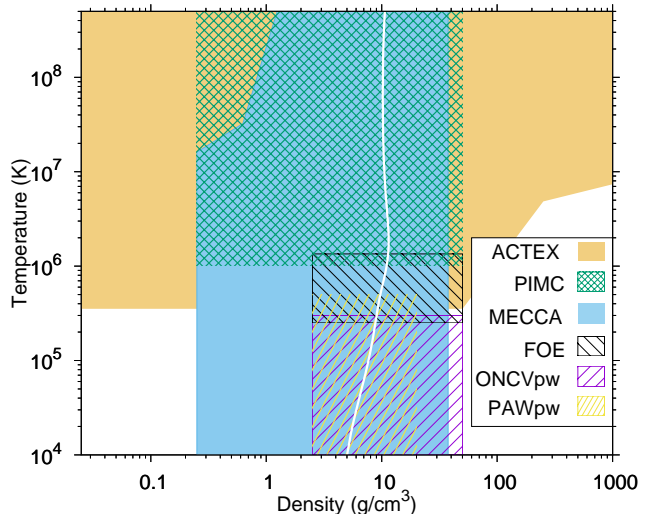


FIG. 1. Schematic diagram showing the temperature-density regions at which different methods are used in this work for calculating the EOS of B₄C. The principle Hugoniot from LEOS 2122 is shown (white curve) for comparison.

spectives; finally we conclude in Sec. VI.

II. COMPUTATIONAL METHODS

In this section, we briefly describe the computational settings of the theoretical methods that we employ to compute the internal energies and pressures of B₄C across wide ranges of temperatures and densities. Figure 1 summarizes the conditions at which each of the methods has been used. The computations are performed by leveraging the applicability, accuracy, and efficiency of each method. More theoretical details can be found in our recent paper¹⁵ and references therein.

We perform PIMC simulations of B₄C using the CUPID code³⁸. All electrons and nuclei are treated explicitly. In order to deal with the Fermionic sign problem, we apply the fixed-node approximation using free-particle nodes to restrict the paths^{39–41}. The pair density matrices^{42,43} are evaluated in steps of $\frac{1}{512}$ Hartree⁻¹ (Ha⁻¹) and the nodal restriction is enforced in steps of $\frac{1}{8192}$ Ha⁻¹. The calculations are performed at densities of 0.25–50.17 g/cm³ [0.1 to 20 times the ambient density ($\rho_0 \sim 2.5$ g/cm³)⁴⁴] and temperatures of 10^6 – 5×10^8 K. Each simulation cell consists of 30 atoms, which is comparable to our previous simulations for pure B, BN, and hydrocarbons^{12,15,45,46}. The finite cell size effects on the EOS are negligible at such high temperature conditions⁴⁷.

Our DFT-MD simulations for B₄C are performed in two different ways. One way is by using the frozen-core projector augmented wave (PAW)⁴⁸ or optimized norm-conserving Vanderbilt (ONCV) pseudopotentials^{49,50} and plane-wave (pw) basis; the other is a

Fermi operator expansion (FOE)^{51,52} approach using all-electron ONCV potentials. The PAWpw calculations are performed using the Vienna *Ab initio* Simulation Package (VASP)⁵³ and employing the hardest available PAW potentials (core radius equals 1.1 Bohr for both B and C), Perdew-Burke-Ernzerhof (PBE)⁵⁴ exchange-correlation functional, a large cutoff energy (2000 eV) for the plane-wave basis, and the Γ point to sample the Brillouin zone. The PAWpw calculations of the EOS are performed at 6.7×10^3 – 5.05×10^5 K (~ 0.6 – 43.5 eV) and 1–10 times ρ_0 . We conducted ONCVpw simulations⁵⁵ at temperatures up to 3×10^5 K, using PBE exchange-correlation functional and a 900 eV energy cutoff (core radius equals 1.125 Bohr for both B and C) for the plane-wave expansion, in order to cross check the PAWpw results. For both PAWpw and ONCVpw calculations, a Nosé thermostat⁵⁶ is used to generate MD trajectories (typically ~ 5000 steps) that form canonical ensembles. The MD time step is chosen within the range of 0.05–0.55 fs, smaller at higher temperatures. Cubic cells with 30 and 120 atoms are considered to eliminate the finite-size errors on the EOS.

We perform FOE calculations at temperatures of 2.5×10^5 – 1.34×10^6 K. Note that FOE takes advantage of the smooth Fermi-Dirac function at high temperature by approximating the function with polynomial expansion, which provides a very efficient way to conduct the Kohn-Sham DFT-MD calculation. We use 30-atom cells and conduct *NVT* simulations that last 3000–6000 steps (0.05–0.1 fs/step) to ensure sufficient statistics to obtain the EOS. To be consistent with the plane-wave calculations, the FOE calculations employ PBE exchange-correlation functional and much larger energy cutoff (4000 eV) due to smaller core radius (0.8 Bohr) due to the inclusion of 1s core states in both B and C pseudopotentials. We also use the all-electron ONCV potentials and pw basis to perform calculations at densities of 12.544 g/cm³ or higher and temperatures of 1.26×10^5 K or lower, in order to reduce the possibility of frozen-core overlap in the MD simulations.

Over the last ten years, Militzer *et al.* have developed and employed the approach combining PIMC and DFT-MD to calculate the EOS of a series of elemental materials (He⁵⁷, B¹², C⁴¹, N⁵⁸, O⁵⁹, Ne⁵⁸, Na^{60,61}, Al⁶², Si⁶³) and compounds (H₂O⁴¹, LiF⁶⁴, CH^{45,46}, BN¹⁵, MgO⁶⁵, MgSiO₃⁶⁶) over wide ranges of temperatures and pressures. The PIMC data were shown to reproduce predictions by classical plasma theories (such as the Debye-Hückel and the ideal Fermi-gas model) in the limit of infinitely high temperatures and agree remarkably well (differences up to $\sim 5\%$) with DFT-MD for the partially ionized, warm dense states at $\sim 10^5$ – 10^6 K (or 10–100 eV), while the DFT-MD predictions of the Hugoniot are consistent with dynamic shock experiments that are available up to multi-megabar (Mbar) pressures. By fully capturing the ionic interaction effects (DFT-MD), nuclear quantum effects (PIMC), and electronic many-body effects (PIMC), these computations set accurate

constraints for the EOS of these materials (Z up to 14) from condensed matter to hot plasma states (degeneracy parameter ~ 0.1 – 10^3 , coupling parameter ~ 0.01 – 10) and serve as benchmarks for the development of other, computationally more efficient EOS methods.

In a recent paper¹⁵, an all-electron, Green’s function KKR electronic-structure method based on Kohn-Sham DFT and an activity expansion method, in addition to FOE and a spectral quadrature method, were used to compute the EOS of BN and compare with the PIMC and pw DFT-MD data. The Green’s function method simplifies the calculation by using a static lattice and approximating the ion kinetic contribution with an ideal gas model, and show good agreement with PIMC and DFT-MD predictions at above 10^5 K when the ion thermal contribution becomes less significant in comparison to electron thermal or cold curve contributions. The activity expansion approach is based on an expansion of the plasma grand partition function in powers of the constituent particle activities (fugacities)^{67,68}, and the EOS calculations include interaction terms beyond the Debye-Hückel, electron-ion bound states and ion-core plasma polarization terms, along with relativistic and quantum corrections^{69,70}, and therefore produce accurate EOS at temperatures down to $\sim 10^6$ K. It is thus interesting to explore the ranges of applicability of these approaches for B₄C.

We use the Multiple-scattering Electronic-structure Calculation for Complex Applications (MECCA) code for the all-electron, Green’s function KKR calculations.⁷¹ The KKR spherical-harmonic local basis included $L_{\max} = 2$ within the multiple-scattering contributions, and L up to 200 are included automatically until the free-electron Bessel functions contribute zero to the single-site wavefunction normalizations. We use local density approximation (LDA)⁷² for the exchange-correlation functional, a $12 \times 12 \times 12$ Monkhorst-Pack⁷³ k -point mesh for Brillouin zone integrations for energies with an imaginary part smaller than 0.25 Rydberg, and a $8 \times 8 \times 8$ k -point mesh otherwise. A denser mesh was used for the physical density of states calculated along the real-energy axes when needed. We use a static 5-atom cubic cell for the calculations and approximate the ion-kinetic contribution by the ideal gas model. This structure can be viewed as a body-centered cubic carbon lattice that has a simple-cubic boron sublattice inscribed at $(\pm 1/4, \pm 1/4, \pm 1/4)$ and $(\pm 3/4, \pm 3/4, \pm 3/4)$. This assumed crystal structure is by no means representable for B₄C at ambient conditions. Therefore, it is not expected to agree with experiments or other computational methods that do not assume this static structure. However, the structure is space filling and might be a representation for higher temperatures and pressures.

Activity expansion calculations are performed using the ACTEX code^{67,68}. We cut off ACTEX calculations at temperatures below the point where many-body terms become comparable to the leading-order Saha term ($T > 5.8 \times 10^5$ K).

III. EXPERIMENTS

We present Hugoniot data for B_4C to 61 Mbar, exceeding the shock pressures achieved in previous experiments³⁵ by a factor of eight. The new data were obtained from experiments at the NIF⁷⁴, where the B_4C Hugoniot was measured relative to a diamond standard using the impedance-matching technique. The planar target package, which was affixed to the side of a laser-driven hohlraum, had a 200- μm -thick diamond ablator, 5- μm -thick gold preheat shield, a 100- μm - or 125- μm -thick diamond baseplate (the impedance-matching standard), and B_4C , diamond, and quartz samples as shown in Fig. 2(a). The surfaces opposite the drive of the diamond baseplate and smaller diamond sample were flash coated with 100 nm of aluminum to facilitate shock break out time measurements. Densities of the polycrystalline diamond, z-cut α -quartz, and B_4C were 3.515 g/cm³, 2.65 g/cm³, and 2.51 g/cm³, respectively. The inner walls of the hohlraum were irradiated with 176 laser beams, which produced a ~ 200 eV x-ray bath that drove a planar and nearly steady shock through the target package. The time-dependent shock velocity history in the quartz, measured using a line-imaging velocity interferometer for any reflector (VISAR)⁷⁵, showed only $\pm 3\%$ variation from the average over the relevant time period of the experiment. The laser pulse duration, either 5 or 7.5 ns, and the total energy, between 519 and 820 kJ, varied shot-to-shot to produce high-pressure states in the B_4C spanning 27 to 61 Mbar.

The shock velocities in the diamond baseplate (standard) and B_4C sample at the material interface are required to determine the pressure-density state on the B_4C Hugoniot using the impedance-matching technique. Average shock velocities through the smaller diamond and B_4C samples were calculated from their thicknesses, measured using a dual confocal microscope, and the shock transit times, measured using VISAR. The *in situ* shock velocities in the B_4C and diamond samples were determined from the measured shock velocity history in the quartz using an analysis technique to correct for shock unsteadiness⁷⁶. The average and *in situ* shock velocities are shown in Fig. 2(b). The Hugoniot and release data for the diamond standard were determined using LEOS 9061, a multiphase EOS for carbon based on DFT-MD and PIMC calculations⁷⁷. The experimental B_4C Hugoniot data are given in Table I. Further details on the experimental configuration and analysis techniques can be found in Ref.⁷⁸, which reports on quartz and molybdenum data that were acquired simultaneously with the B_4C data presented here.

IV. RESULTS AND DISCUSSION

A. Hugoniot comparison

In this section, we compare our experimental measurements of the pressure-density Hugoniot of B_4C with our theoretical predictions. Figure 3 compiles the experimental and theoretical Hugoniot curves in pressure-density and temperature-density plots.

The comparison in Fig. 3 shows very good consistency between the measurements and the theoretical predictions. Assisted by the theoretical predictions, we estimate Hugoniot temperatures for the experimental data to be in the range of $1\text{--}5 \times 10^5$ K. Our results also show that the PIMC and DFT-MD predicted Hugoniot are in overall good consistency with LEOS 2122 (L2122). Our calculations and the L2122 model predicts B_4C to have a maximum compression ratio of 4.55 at 9×10^2 Mbar and 2×10^6 K, below which L2122 predicts B_4C to be slightly softer. We also note that the pressure-density Hugoniots predicted by a different Thomas-Fermi based tabular model L2120 is very similar at pressure ranges other than that around the compression maximum, at which the L2120 prediction is stiffer by $\sim 6\%$. This can be attributed to the K-shell ionization that is fully captured by our calculations and the Purgatorio model L2122, while no atomic shell effects has been included in Thomas-Fermi models. In comparison, another Thomas-Fermi table (SESAME 7082), although reasonably agreeing with the low-pressure OMEGA data, can be clearly ruled out by our NIF data and computations. This may be attributed to the inaccuracies in the cold curve and the ion thermal model used in the table. The latest NIF gigabar (Gbar) experiments obtain Hugoniots of CH and B near the compression maxima that agree with our PIMC calculations better than Thomas-Fermi predictions.⁷⁹ We expect future, accurate experiments at Gbar pressures to test our predictions for B_4C .

At 3–400 Mbar and $10^4\text{--}10^6$ K, the Hugoniot curve obtained from MECCA and those from DFT-MD (PAWpw, ONCVpw, and FOE) agree remarkably well with each other. Because MECCA calculations are based on a static lattice and the ion thermal contribution to the EOS is added following an ideal gas model, the good consistency implies that the ion thermal contribution is dominated by the ion kinetic effect. We note that AC-TEX predictions of the Hugoniot down to 6×10^5 K and 140 Mbar also agree very well with the DFT predictions.

The computational predictions are consistent with the NIF experimental data at pressures above 27 Mbar, as well as those conducted at the Omega laser facility³⁵ up to 5 Mbar. However, at 5–10 Mbar, the experimental Hugoniot seems to be softer than DFT-MD predictions, similar to findings by a previous DFT-MD study that was performed up to 15 Mbar³⁶, which might be attributed to chemical separation of the B_4C samples as has been carefully explored for solid B_4C at low temperatures in Ref. 36.

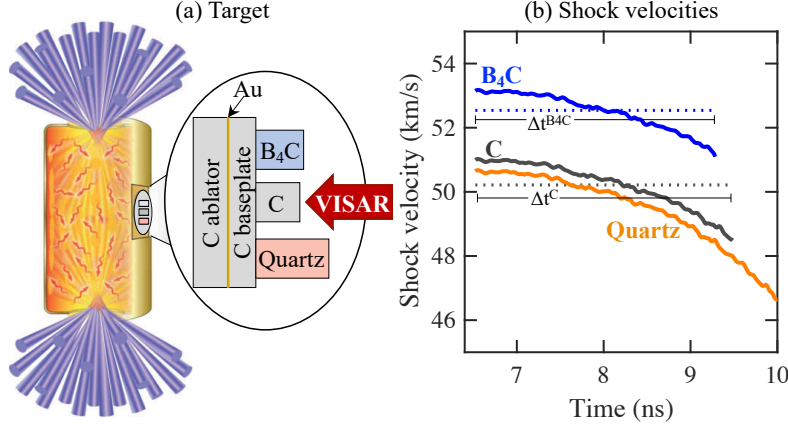


FIG. 2. (a) Target design and (b) shock velocities in the boron carbide (B_4C), diamond (C), and quartz samples attached to the diamond baseplate for NIF shot N160414. Dotted lines in (b) show the average shock velocity in the samples determined from the measured thickness and shock transit time (Δt). Solid curves show the time-dependent shock velocity histories, measured using VISAR for quartz (orange) and determined using the nonsteady waves correction for B_4C (blue) and diamond (gray).

TABLE I. B_4C Hugoniot data using the impedance-matching technique with a diamond standard. Shock velocities (U_s) at the diamond standard/sample interfaces were measured *in situ* using VISAR for quartz (Q) and determined using the nonsteady waves correction for B_4C and diamond (C). U_s^C and $U_s^{B_4C}$ were used in the impedance-matching analysis to determine the particle velocity (u_p), pressure (P), and density (ρ) on the B_4C Hugoniot. The average shock velocities ($\langle U_s \rangle$) determined from the measured thickness and shock transit times are also listed. The uncertainties for $\langle U_s \rangle$ are the same as those given for U_s .

Shot #	U_s^Q (km/s)	$\langle U_s^C \rangle$ (km/s)	U_s^C (km/s)	$\langle U_s^{B_4C} \rangle$ (km/s)	$U_s^{B_4C}$ (km/s)	$u_p^{B_4C}$ (km/s)	P^{B_4C} (Mbar)	ρ^{B_4C} (g/cm ³)
N160414	50.65 ± 0.25	50.22	51.00 ± 0.35	52.54	53.15 ± 0.46	36.86 ± 0.39	49.38 ± 0.59	8.22 ± 0.29
N161002	56.57 ± 0.25	55.35	56.43 ± 0.50	57.43	58.63 ± 0.43	41.60 ± 0.55	61.46 ± 0.86	8.68 ± 0.35
N170227	44.30 ± 0.25	44.61	45.39 ± 0.33	46.77	47.62 ± 0.30	31.98 ± 0.36	38.38 ± 0.46	7.67 ± 0.22
N170503	38.17 ± 0.25	38.62	39.18 ± 0.29	39.65	40.38 ± 0.25	26.84 ± 0.31	27.31 ± 0.33	7.52 ± 0.21
N170808	51.22 ± 0.25	50.38	51.13 ± 0.41	53.22	54.04 ± 0.36	36.82 ± 0.45	50.15 ± 0.65	7.91 ± 0.25
N180411	43.98 ± 0.25	44.49	45.05 ± 0.37	46.56	47.15 ± 0.44	31.72 ± 0.40	37.67 ± 0.52	7.70 ± 0.28
N180611	39.67 ± 0.25	39.27	40.60 ± 0.40	40.68	42.15 ± 0.25	28.00 ± 0.43	29.74 ± 0.47	7.51 ± 0.26

We note that, at temperatures of $1\text{--}4 \times 10^6$ K, our PIMC data for B_4C have large errors (up to $\sim 2\%$) because of the large computational cost and stochastic noise at these conditions. The error quickly drops down with increasing temperature. We use a Monte Carlo approach to estimate the associated uncertainty in density along the Hugoniot by taking into account the errors in the PIMC data. The results are shown with the green shaded area in Fig. 3. It is clear that the PIMC Hugoniot is in excellent agreement with L2122 predictions and is consistent with those predicted by ACTEX and MECCA within the error bar. Slight differences of up to 2–3% can be observed at 400–10,000 Mbar and $10^6\text{--}10^7$ K. This may be due to the methodological difference between ACTEX/MECCA and PIMC/Purgatorio.

In order to better understand the origin of the differences at the compression maximum, we compare in Fig. 4 the energy term $E - E_i$ and the pressure term $(P + P_i)(V_i - V)/2.0$, where (E, P, V) and (E_i, P_i, V_i) respectively denote the internal energy, pressure, and vol-

ume of B_4C under shock and in its initial state (300 K and 2.51 g/cm³), of the Hugoniot function from PIMC, ACTEX, MECCA, and LEOS 2122 along two isotherms 1.3×10^6 K and 2×10^6 K. The cross point between the curve of the energy term and that of the pressure term gives the Hugoniot density at the corresponding temperature. Our comparison shows that the internal energy slowly decreases while the pressure term dramatically increases, as the density increases from 9 to 14 g/cm³.

Due to the high computational expense of PIMC simulations at low-temperature conditions, our PIMC data at low temperatures exhibit significantly larger error bars and stochastic noise than the higher temperature results. The error bars of the PIMC data lead to estimations of the 1σ uncertainty in Hugoniot density, as is shown with shaded green areas in Fig. 3. L2122 and PIMC agree well with each other in both energy and pressure, explaining the excellent consistency between their predicted Hugoniot. MECCA pressures are slightly higher than PIMC, whereas energies are similar, therefore the Hugoniot den-

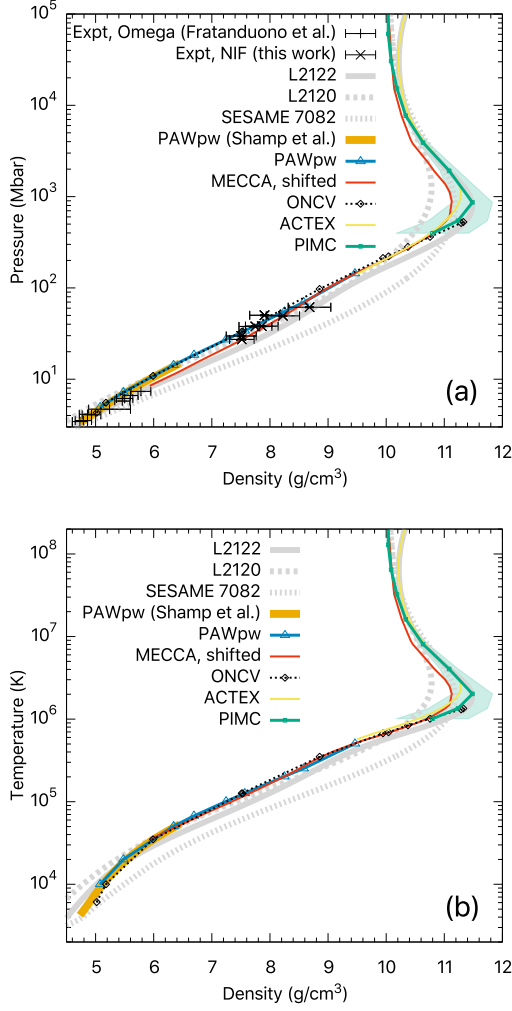


FIG. 3. Comparison of the Hugoniot of B_4C predicted by various simulations and the LEOS/SESAME models in (a) pressure-density and (b) temperature-density representations. Also shown in (a) is our experimental data collected at the NIF and those by Fratanduono *et al.*³⁵ at Omega laser facility. The shaded areas around the lower end of the PIMC curve represent 1σ uncertainty in the corresponding Hugoniot density due to EOS errors. All pressures in our MECCA EOS table have been shifted up by 97.1 GPa, so that the value at ambient is zero. The deviation between PIMC/L2120 (and MECCA) and ACTEX/L2122 curves above 10^4 Mbar is due to the electron relativistic effect, which is considered in ACTEX and L2122 but not in PIMC/L2120 (and not fully in MECCA). The initial sample density $\rho_i = 2.51 \text{ g/cm}^3$ for all the Hugoniot except that by Shamp *et al.*³⁶, which is 2.529 g/cm^3 .

sity is also lower. In comparison to PIMC, ACTEX energies are lower, while pressures are similar at $1.3 \times 10^6 \text{ K}$ but lower at $2 \times 10^6 \text{ K}$, therefore the Hugoniot densities from ACTEX are also lower.

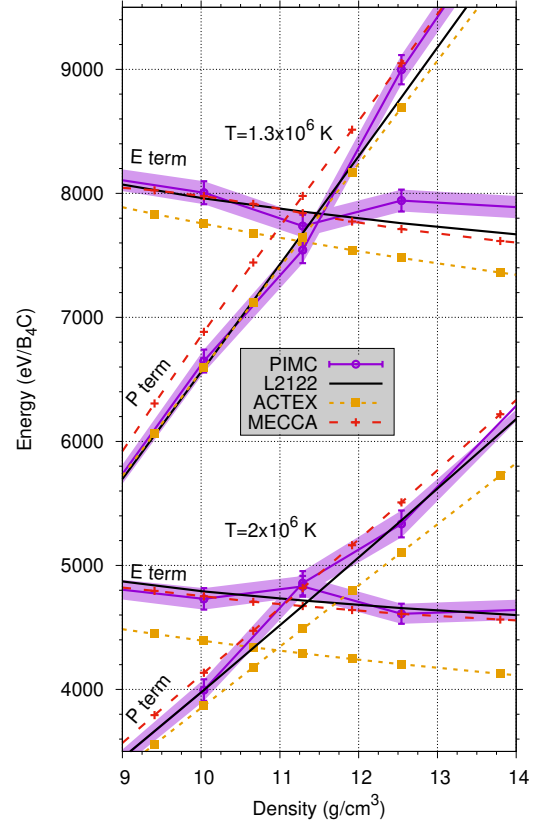


FIG. 4. Comparison of the energy and pressure terms of the Hugoniot function for B_4C from different theories and EOS models at two temperatures around the compression maximum. The shaded area denote the standard error of the PIMC EOS.

B. EOS comparison

The principle Hugoniot samples a specific pathway in the phase space from 2.5 to 11.5 g/cm^3 accompanied by increasing temperatures. These conditions are very important because the corresponding states are reachable using shock experiments. However, off-Hugoniot states, as those simulated in the present work, also play vital role in hydrodynamic simulations and the underlying physics can be different. We therefore make detailed comparisons of the EOS among various methods in this subsection.

The pressure-temperature data along several isochores from our calculations are compared in Fig. 5. At $4 \times 10^6 \text{ K}$ and above, all our methods (PIMC, ACTEX, and MECCA) agree and are consistent with the L2122 model. This is understandable because the system is approaching the limit of a fully-ionized classical plasma, which is accurately described by PIMC, ACTEX, and the DFT methods MECCA and Purgatorio.

At lower temperatures, the different ways of employing DFT-MD (PAWpw, ONCVpw, and FOE) give the same EOS and consistent trend with the PIMC data. Several differences are noteworthy when other methods

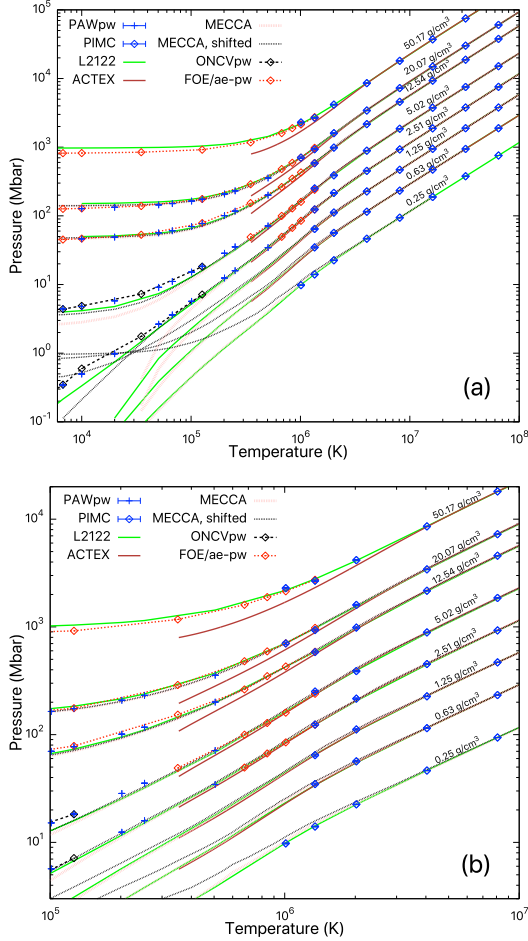


FIG. 5. Comparison of the pressure-temperature profiles of B_4C along several isochores from PIMC, DFT-MD [PAWpw, frozen 1s; ONCVpw, frozen 1s; FOE or pw, all-electron(ae)], ACTEX, MECCA, and L2122. Also included is a set of MECCA data that have been shifted up by 97.1 GPa, so that the value at ambient is zero. Subplot (b) is a zoom-in version of (a).

(ACTEX, MECCA, and L2122) are considered: (1) ACTEX pressures being lower than others, more so at higher densities; (2) MECCA pressures being significantly different from L2122 at 5 g/cm³ and below, in particular at $T < 10^5$ K; (3) with a rigid shift-up of 97.1 GPa (so that the ambient pressure is zero), MECCA pressures agree better with L2122 at ambient density and above, but worse at lower-than-ambient densities; and (4) FOE pressures gets slightly lower than L2122 for densities higher than 25 g/cm³.

Figure 6 focuses on the differences between the first-principles PIMC/DFT-MD data and L2122 $\Delta P = (P^{FP} - P^{L2122})/P^{L2122} \times 100\%$. The agreement is well within 3% for all densities studied presently and temperatures above 4×10^6 K. At lower temperatures, ΔP varies between $\pm 17\%$ depending on the density—DFT-MD pressures are in general higher at densities below 10 g/cm³ and lower above. $|\Delta P|$ becomes smaller than

10% and gradually vanishes when temperature increases to 3.5×10^5 K or above. PAWpw and ONCVpw/FOE predictions are overall the same. FOE smoothly bridges with PIMC predictions at 10^6 K.

We also compare the pressures and energies from our different computations with those from L2122. The results along two isotherms 1.3×10^6 and 2×10^6 K are shown in Fig. 7. We find that PIMC, MECCA, and FOE agree with each other to within 5%, which is comparable to what we found about differences between PIMC and DFT-MD in previous work on B¹², BN¹⁵, and hydrocarbon systems^{45,46}. The cross validation of the different DFT methods and their consistency with PIMC predictions confirm that both the PIMC and the DFT-MD approaches, albeit carrying approximations in each, are reliable for studying the EOS of warm dense matter. Our ACTEX data also show remarkable consistency (e.g., $< 2\%$ at 2×10^6 K) with L2122 at densities below 10 g/cm³. However, the ACTEX data get way too low at higher densities, which is due to breakdown of the ACTEX method when the two-body term at order 2 in the activity becomes comparable to the Saha term, similar to what has been found for BN¹⁵.

C. Modifications to L2122 and 1D hydrodynamic simulations

We have shown in Fig. 3 that L2122 predicts slightly softer behavior for B_4C at 5–500 Mbar, despite the overall good consistency, in comparison with our first-principles and experimental Hugoniot. We have thus created three new models for the B_4C EOS, with the intent to span the range of Hugoniot behavior that is in better agreement with the experimental data from both NIF and Omega. Recent advances in ICF design methodologies that leverage Bayesian inference techniques to find most probable physics models based on a range of experimental outcomes⁸⁰ and recent interest in B_4C as an ablator for such experiments motivated us to create this range of possible EOS models rather than just a single table. By considering the range of reasonable EOS models for B_4C as obtained from our above comparisons of theoretical methods and experimental uncertainty, we developed these three new tables by making modifications to the Grüneisen parameter within the QEOS methodology.

The Hugoniot curves corresponding to the new models (L2123, L2124, and L2125) are shown in Figure 8, along with the experimental data. The PIMC Hugoniot with error bars is also shown. The new baseline model (L2123) has a slight modification to the Grüneisen parameter, which determines the ion thermal EOS, to bring it into better agreement with both sets of experimental data. L2124 and L2125 have modified forms of the Grüneisen parameter that span the range of the experimental error bars. Both L2123 and L2124 (the softer model) closely track L2122 near peak compression, whereas the L2125

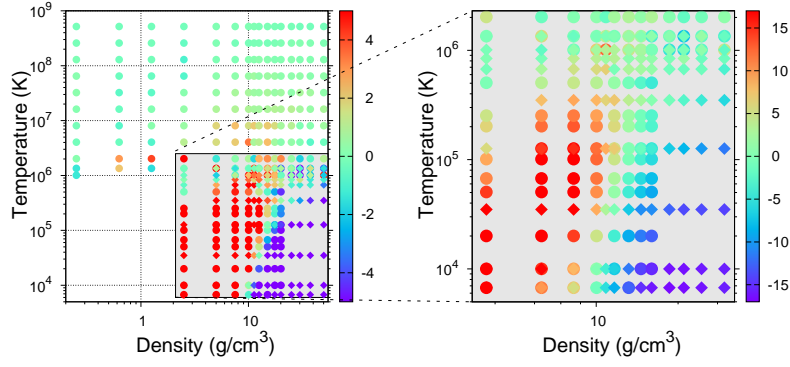


FIG. 6. Percent difference in pressure of B_4C between PIMC/PAWpw (in spheres) or ONCV (in diamonds) and L2122.

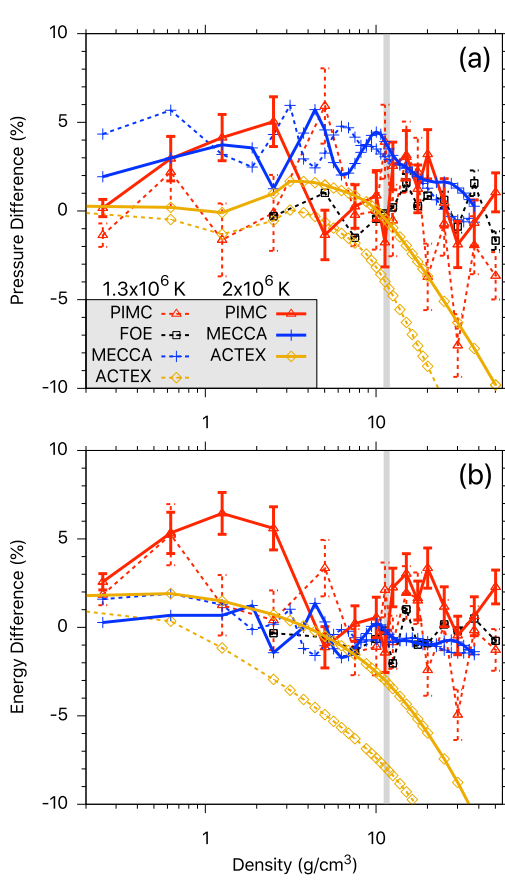


FIG. 7. EOS differences of PIMC (red), FOE (black), MECCA (blue), and ACTEX (yellow) relative to LEOS 2122 along two isotherms [1.3×10^6 (dashed curves) and 2.0×10^6 K (solid curves)]. Because of the different references chosen in the EOS datasets, all energies have been shifted by the corresponding values at ambient condition (2.5087 g/cm^3 and 300 K). The pressure differences are normalized by the corresponding LEOS 2122 values; the energy differences are normalized by the fully-ionized ideal gas values ($46.5 k_B T$ per B_4C). The statistical error bars correspond to the 1σ uncertainty of the FOE and PIMC data. The gray vertical bar at 11.54 g/cm^3 denotes the maximum Hugoniot density according to LEOS 2122 and PIMC.

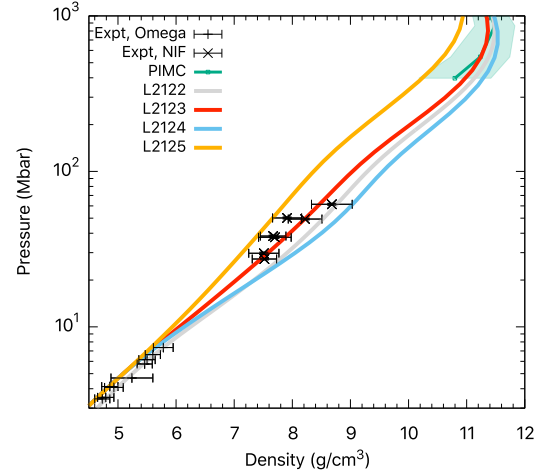


FIG. 8. Comparison of the Hugoniot ($\rho_i = 2.51 \text{ g/cm}^3$) of B_4C from newly constructed QEOS models (L2123, L2124, and L2125) and those from experiments, PIMC simulations, and L2122.

(the stiffer model) shows significantly modified behavior near peak compression.

We applied these new models to 1D hydrodynamic simulations of a polar direct drive fusion experiment based on previous studies.^{18,81} For this study, we kept the capsule diameter constant at $3000 \mu\text{m}$ and set the gas pressure to 8 atm of D_2 at room temperature. We used a flux limiter=0.0398 and a square pulse shape with peak power set to 280 TW. The pulse duration was chosen such that 476 kJ of energy would be available from the laser. Due to geometric losses, we assumed that the maximum absorption of energy would correspond to 75 % of the total energy available. Similar to our previous work on boron¹², we found that the EOS variations we considered here did not produce significant differences in the fuel areal density, peak ion temperature, or ablator areal density in these direct drive simulations.

In order to expand this sensitivity study to situations that might be more relevant to future neutron source de-

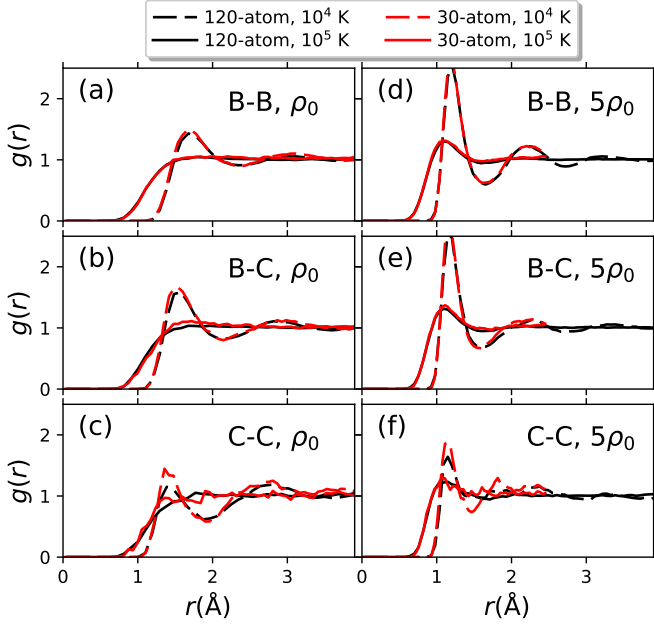


FIG. 9. Comparison of the nuclear pair correlation function obtained from DFT-MD (PAWpw) for B_4C using 30-atom (red) and 120-atom (dark) cells at two different densities and two temperatures. The reference density ρ_0 is 2.5087 g/cm^3 .

velopment studies,⁸² we also examined the neutron yield vs. ablator thickness for each of the three EOS models. Interestingly, all four EOS models (L2122–L2125) predict similar profiles for the neutron yield with a peak yield that occurs around an ablator thickness of $7.5 \mu\text{m}$. Differences between the models are all within 1% for thin ($<10 \mu\text{m}$) ablators. For ablator thickness between 10 – $25 \mu\text{m}$, we found the neutron yield from L2123 remains similar ($<0.2\%$), while that from L2124 and L2125 deviate by up to 3%, in comparison to L2122. These results demonstrate the availability of these models for use in future studies in ICF design with novel ablators.

V. DISCUSSION

For the sake of benefiting future EOS development, high energy density physics, and warm dense matter studies, we hereafter discuss the physical origins of the EOS differences shown above from electronic-structure and QEOS points of view.

A. Finite size effects

Our first-principles calculations PIMC, PAWpw, ONCVpw, and FOE implement the standard way of simulating liquids⁸³, which considers a finite number of atoms in a cubic box and under the periodic boundary condition. The finite-cell size effects have been carefully addressed in

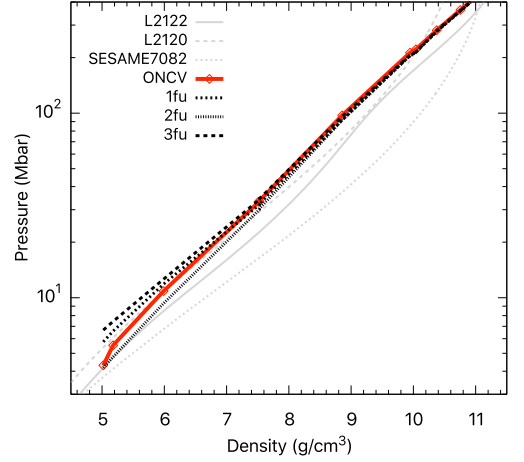


FIG. 10. Comparison of pressures from single-snapshot calculations using various cells [1 formula unit (fu): 5-atom cell; 2 fu: 10-atom cell; 3 fu: 15-atom cell] at the ONCV Hugoniot densities and temperatures. The Hugoniot from three EOS models are also shown for comparison.

our DFT-MD simulations by choosing large-enough cells with 120 atoms for all temperatures up to $2.5 \times 10^5 \text{ K}$ ($\sim 20 \text{ eV}$). This is much higher than the chemical bonding (typically about a few eV) is allowed, which justifies the usage of 30-atom cells for all simulations at higher temperatures. In order to show this, Fig. 9 compares the nuclear pair correlation function at two different temperatures (10^4 and 10^5 K) and two different densities (2.5 and 12.5 g/cm^3) using two different cells sizes (30 and 120 atoms), from our PAWpw calculations. The results show remarkably good agreement in the features of $g(r)$ using 30-atom cells with those using the much larger 120-atom cells even at the relatively low-temperature (10^4 K), high-density (12.5 g/cm^3) condition. This is different from our recent findings for BN, which show stronger size dependence at similar conditions, and is probably due to larger polarization effects in BN than in B_4C . Moreover, structures can be clearly seen in the pair correlation plot at 10^4 K , which are signatures of chemical bonding. At 10^5 K , these structures smooth out and the $g(r)$ becomes more ideal-gas like, which validates the ideal mixing approximation in multi-component average-atom EOS approaches^{45,46}.

At temperatures below 10^5 K , chemical bonding has to be described using reasonably big simulation cells so that the EOS can be accurately obtained. In Sec. IV B, we show that MECCA calculations using a 5-atom cell produce a pressure (-97.1 GPa) that is significantly different from 1 bar at ambient condition, and therefore a rigid shift in pressure for the MECCA EOS table has to be applied to improve the agreement between MECCA and DFT-MD Hugoniots. It is worthwhile to investigate the effect of using such small sizes in more depth by making comparisons with slightly larger ones.

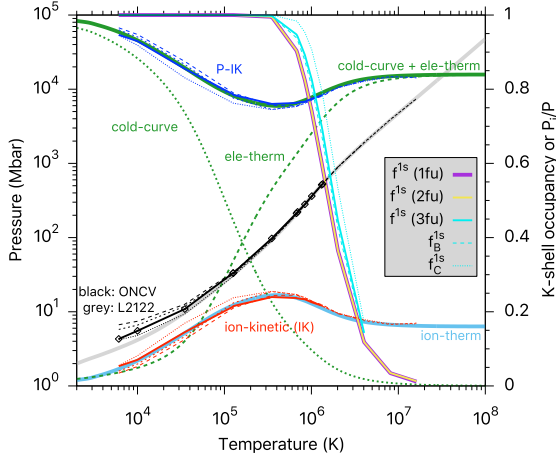


FIG. 11. Fractional decomposition of pressure (right axes) in the LEOS 2122 model and ONCV calculations along their respective Hugoniot (black/grey curves, left axes). Also shown are the K-shell occupancy (right axes) of boron and carbon atoms and the average values as obtained from ONCV calculations using different cell sizes (shown in the legend). The ONCV pressures calculated at the Hugoniot temperature and density conditions and using smaller cells [short dashed: 1 formula unit (fu) (5-atom cell); dotted: 2 fu (10-atom cell); dashed: 3 fu (15-atom cell)] are shown for comparison.

We constructed three structures consisting of 5, 10, and 15 atoms respectively⁸⁴, and performed additional pw-based single-snapshot calculations using all-electron ONCV potentials along the density-temperature Hugoniot predicted using the ONCVpw/FOE EOS. The pressure data as a function of density from the new ONCV calculations are compared in Fig. 10). The results show that using 10-atom cells brings the pressure down relative to that using 5-atom cells. However, using larger, 15-atom cells leads pressure to the opposite direction, instead of approaching the converged values. The differences as signatures of ion thermal and cold-curve effects on the EOS of B_4C are observable along the Hugoniot at densities up to 9 g/cm^3 , which is $\sim 100 \text{ Mbar}$ and $\sim 3 \times 10^5 \text{ K}$.

B. Roles of kinetic and interaction effects from ions and electrons

In order to clarify the roles of kinetic and interaction effects and those from the ions and from the electrons, we performed additional analysis of our pw-based all-electron ONCV calculations. The calculations allow decomposing the total pressure into an ion-kinetic (IK) term, which is calculated using the ideal gas model, and a remaining term (P-IK)(Fig. 11). In comparison to the QEOS way of decomposing the L2122 Hugoniot pressure into ion-thermal, electron-thermal, and cold curve components, we find that the IK contribution is overlapping

with the ion-thermal term in L2122.

In addition, we find that the temperatures at which finite cell size effects are significant, as characterized by the differences between solid and dashed curves, overlap with those at which the cold-curve surpasses the ion-thermal contributions. The turn-over point T_t , $\sim 3 \times 10^5 \text{ K}$ for B_4C , may be interpreted as a conservative estimation of the uppermost temperature at which finite-size effect remains significant in a theoretical computation, or the lowermost temperature at which an average-atom approach is feasible. Below T_t , interactions are so significant that the ideal mixing approximation becomes less reliable and a large simulation cell is required for the accuracy of computations.

As temperature increases to a critical value T_c where K-shell ionization starts, the electron-thermal contribution becomes dominant. This leads to a saddle point in the IK and the P-IK curves in Fig. 11. Our present calculations show $T_c = 3 \times 10^5 \text{ K}$ for B_4C , which is close to what we previously obtained for pure boron¹² and slightly below that for carbon. This is not unexpected because the K level is deeper for elements with higher Z . At temperatures above $\sim 2 \times 10^7 \text{ K}$, B_4C is fully ionized and the EOS is dominated by ideal-gas contributions from the nuclei and the electrons.

In order to further elucidate the roles of interaction and kinetics in the EOS, we calculate their respective contributions to the heat capacity C_V along the Hugoniot using the all-electron ONCV potential, and the results are shown in Fig. 12(a). The ion kinetic term (K_{ion}) contributes $7.5k_B/B_4C$ to C_V independent of temperature, where k_B is the Boltzmann constant. Electron kinetic contributions (K_{ele}) are generally higher (above $15k_B/B_4C$) and show two bumps, one at 10^4 K and the other at 10^6 K , which can be attributed to the L- and the K-shell ionization, respectively. In contrast to K_{ion} which follows an ideal gas model at all temperatures, K_{ele} is dependent on both the electronic orbitals and their occupancy, instead of purely on ionization, and is not ideal gas-like until the system is fully ionized. This can be seen from its asymptotically approaching the ideal gas value of $39k_B/B_4C$ at above $4 \times 10^6 \text{ K}$.

The interaction effects on the EOS are more complicated and consist of contributions by ion-ion (“Ewald”), electron-ion (“external”), and electron-electron (“exchange-correlation” and “Hartree”) interactions. For simplicity of EOS discussions, it might be easier to group them together than to present individually. This is clearly shown by the difference between the red (K_{ele}) and the blue ($E - K_{\text{ion}}$, meaning all except ion kinetic contributions) line-points in Fig. 12(a). The net effect of interactions can be categorized into two regions: I (gray shaded) is below $\sim 10^5 \text{ K}$ with $K_{\text{ele}} > E - K_{\text{ion}}$ and implying negative net contribution of interaction to C_V ; II (yellow shaded) is above $\sim 10^5 \text{ K}$ with $K_{\text{ele}} < E - K_{\text{ion}}$ implying positive contributions of interaction to C_V .

At $\sim 6 \times 10^3 \text{ K}$, K_{ele} contributions are largely offset by electron-electron and ion-ion repulsion, therefore

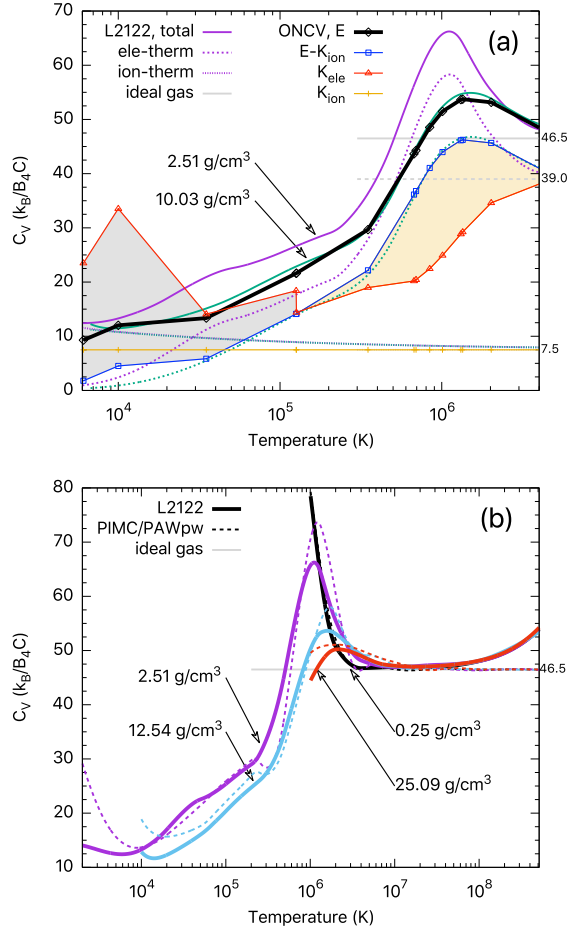


FIG. 12. (a) Decomposition of the heat capacity from LEOS 2122 along two isochores [2.51 g/cm^3 (purple) and 10.03 g/cm^3 (green)] and ONCV along the Hugoniot. (b) Heat capacity comparison between LEOS 2122 and PIMC/PAWpw in a broader range of temperatures. In (a), LEOS 2122 results are decomposed into electron-thermal (short dashed curves) and ion-thermal (thick dotted curves) terms. ONCV data (dark line-points) are decomposed into ion kinetic (yellow), electron kinetic (red), and interaction (i.e., all-except-ion kinetic, in blue) terms.

C_V is dominated by K_{ion} . As temperature increases, the repulsive contribution is gradually offset by the electron-ion attraction, therefore the net interaction contribution gradually increases to zero at $\sim 1.5 \times 10^5 \text{ K}$ and becomes positive at higher temperatures where K-shell ionization occurs. At above $4 \times 10^6 \text{ K}$, K_{ele} and K_{ion} contributions dominate because the system is fully ionized.

Figure 12(a) also compares C_V along several isochores from L2122. As a QEOS model, L2122 decomposes the free energy into three terms: cold-curve, ion-thermal, and electron-thermal. The ion-thermal term (dotted lines) includes both kinetic and interaction effects such as those from vibration. This explains their differences relative to the K_{ion} curves, as well as the consistency between the electron thermal (dashed lines) and $E - K_{\text{ion}}$ (blue line-

points), because the cold curve does not contribute to C_V . We also note [Fig. 12(b)] that the C_V curves from our PIMC/PAWpw calculations in the broad temperature range are consistent with L2122 predictions, except for temperatures above $2 \times 10^7 \text{ K}$, because the electron relativistic effect that is included in the L2122 model raises the internal energy and heat capacity and shifts the Hugoniot toward the limit of 7 times compression at infinitely high temperature.

VI. CONCLUSIONS

In this work, we present a comprehensive study of the EOS of B_4C over a wide range of pressures and temperatures by implementing several computational methods, including PIMC, DFT-MD using standard plane-wave basis and PAW or ONCV pseudopotentials, ACTEX, and MECCA.

Our EOS data by PIMC, FOE, ACTEX, and MECCA show good consistency at 10^6 K where 1s electrons are ionized. Our detailed EOS comparison provides strong evidences that cross validate both the PIMC and the DFT-MD approaches for EOS studies of the partially ionized, warm-dense plasmas.

At $2.5\text{--}3.2 \times 10^6 \text{ K}$ and $1.0\text{--}1.3 \times 10^3 \text{ Mbar}$, our PIMC, ACTEX, and MECCA calculations uniformly predict a maximum compression of ~ 4.55 along the shock Hugoniot for B_4C ($\rho_i = 2.51 \text{ g/cm}^3$), which originates from K shell ionization. This compression is underestimated by TF models by ~ 0.2 (6%). The maximum compression ratio is similar to those of h-BN ($\rho_i = 2.26 \text{ g/cm}^3$)¹⁵ and slightly smaller than pure boron ($\rho_i = 2.31 \text{ g/cm}^3$)¹².

We also report Hugoniot data up to $\sim 61 \text{ Mbar}$ from experiments at the NIF. The measured data show good agreement with our theoretical predictions based on DFT-MD.

By comparing QEOS models with the electron thermal term constructed in different ways (Purgatorio in LEOS 2122 or TF in LEOS 2120/SESAME 7082), we find that the Purgatorio-based EOS models provide excellent overall agreement with our numerical simulations, similar to our previous studies on pure boron and BN. Because the largest differences in the Hugoniot response of the models occurs near peak compression, performing experiments for materials near peak compression^{4,85–88} would provide a rigorous experimental test of our understanding of electronic structure in high energy density plasmas. It would also be worthwhile to pursue experiments that provide measurements of the temperature and the pressure in either Hugoniot or off-Hugoniot experiments, which would provide data to test the first principle calculations.

Based on the experimental data, we have developed three new EOS models (L2123, L2124, and L2125) by variations of the ion thermal EOS model to span the range of experimental error bars. These models were developed to span the range of EOS models that are consistent with the experimental error bars. 1D hydrodynamic

simulations of direct drive implosions with a B₄C ablator demonstrate that the nominal polar direct drive exploding pusher design is not sensitive to the equation of state model. Our work should motivate similar studies for future ICF designs using B₄C ablators.

VII. SUPPLEMENTARY MATERIAL

See the supplementary material (Table II) for the EOS data table of B₄C from this study.

ACKNOWLEDGMENTS

This work was in part performed under the auspices of the U.S. Department of Energy by Lawrence Livermore National Laboratory under Contract No. DE-AC52-07NA27344. Computational support was provided by LLNL high-performance computing facility (Quartz) and

the Blue Waters sustained-petascale computing project (NSF ACI 1640776). B.M. is supported by the U. S. Department of Energy (grant DE-SC0016248) and the University of California. S.Z. is partially supported by the PLS-Postdoctoral Grant of LLNL.

This document was prepared as an account of work sponsored by an agency of the United States government. Neither the United States government nor any agency thereof, nor any of their employees, makes any warranty, express or implied, or assumes any legal liability or responsibility for the accuracy, completeness, or usefulness of any information, apparatus, product, or process disclosed, or represents that its use would not infringe privately owned rights. Reference herein to any specific commercial product, process, or service by trade name, trademark, manufacturer, or otherwise does not necessarily constitute or imply its endorsement, recommendation, or favoring by the U.S. Government or any agency thereof. The views and opinions of authors expressed herein do not necessarily state or reflect those of the U.S. Government or any agency thereof, and shall not be used for advertising or product endorsement purposes.

TABLE II: **Supplementary Material:** first-principles equation of state data for B₄C based on PIMC and DFT-MD [PAWpw, ON-CVpw(1.07), FOE/ae-pw(2.06)] simulations by Burkhard Militzer, Shuai Zhang and Lin H. Yang. Energies are relative to the corresponding values of B₄C at ambient condition (300 K, 2.51 g/cc).

ρ (g/cm ³)	T (K)	P (GPa)	P_{error} (GPa)	E (Ha/B ₄ C)	E_{error} (Ha/B ₄ C)	note
0.2509	1010479	978.3	9.7	206.906	1.219	PIMC_A3368
0.2509	1347305	1402.8	9.4	283.310	1.184	PIMC_A3367
0.2509	2020958	2254.4	10.9	404.807	1.372	PIMC_A3366
0.2509	4041916	4641.0	15.3	711.485	1.926	PIMC_A3365
0.2509	8083831	9400.4	18.0	1312.607	2.266	PIMC_A3364
0.2509	16167663	18839.9	20.1	2501.695	2.528	PIMC_A3363
0.2509	32335325	37744.2	28.3	4881.135	3.559	PIMC_A3362
0.2509	64670651	75667.1	38.4	9653.671	4.832	PIMC_A3361
0.2509	129341301	151298.9	50.4	19170.798	6.348	PIMC_A3360
0.2509	258682602	302675.0	70.6	38219.473	8.871	PIMC_A3359
0.2509	517365204	605430.7	65.9	76316.150	8.280	PIMC_A3358
0.6272	1347305	3476.4	68.1	266.271	3.426	PIMC_A3565
0.6272	2020958	5653.7	69.0	395.583	3.473	PIMC_A3564
0.6272	4041916	11487.2	59.9	700.416	3.015	PIMC_A3563
0.6272	8083831	23286.6	79.8	1298.108	4.016	PIMC_A3562
0.6272	16167663	47143.0	85.3	2500.912	4.296	PIMC_A3561
0.6272	32335325	94249.1	112.8	4873.197	5.674	PIMC_A3560
0.6272	64670651	188925.7	154.8	9639.451	7.786	PIMC_A3559
0.6272	129341301	378160.5	174.2	19164.543	8.762	PIMC_A3558
0.6272	258682602	756073.9	270.9	38186.621	13.628	PIMC_A3557
0.6272	517365204	1513078.5	253.9	76289.408	12.782	PIMC_A3556
1.2544	1347305	6449.7	134.8	238.128	3.390	PIMC_A3576
1.2544	2020958	11170.0	140.0	381.263	3.522	PIMC_A3575
1.2544	4041916	22672.4	119.1	686.744	3.000	PIMC_A3574
1.2544	8083831	46886.6	158.6	1301.944	3.988	PIMC_A3573
1.2544	16167663	94533.2	157.3	2504.194	3.960	PIMC_A3572
1.2544	32335325	188899.6	214.1	4880.955	5.392	PIMC_A3571
1.2544	64670651	378262.2	264.7	9647.721	6.666	PIMC_A3570
1.2544	129341301	757312.8	382.3	19187.998	9.627	PIMC_A3569
1.2544	258682602	1514056.9	533.5	38232.909	13.454	PIMC_A3568
1.2544	517365204	3026294.1	690.7	76291.346	17.394	PIMC_A3567

continued ...

... continued

ρ (g/cm ³)	T (K)	P (GPa)	P_{error} (GPa)	E (Ha/B ₄ C)	E_{error} (Ha/B ₄ C)	note
2.5087	2000	8.8	0.3	0.178	0.001	PBE_B4C120_0137
2.5087	6736	34.2	0.2	0.451	0.000	PBE_B4C120_0138
2.5087	10000	49.7	0.2	0.593	0.001	PBE_B4C120_0139
2.5087	20000	98.2	0.2	1.060	0.001	PBE_B4C120_0140
2.5087	50523	264.2	0.4	2.906	0.001	PBE_B4C120_0141
2.5087	67364	360.7	0.5	4.102	0.002	PBE_B4C120_0142
2.5087	101047	568.4	0.7	6.747	0.003	PBE_B4C120_0143
2.5087	202095	1241.3	1.0	15.738	0.010	PBE_B4C120_0145
2.5087	252619	1590.9	1.5	20.516	0.012	PBE_B4C120_0146
2.5087	505239	3447.0	1.4	45.647	0.020	PBE_B4C30_0019
2.5087	1347305	12396.6	265.9	215.509	3.347	PIMC_A3587
2.5087	2020958	21582.0	288.2	357.506	3.625	PIMC_A3586
2.5087	4041916	45205.4	248.0	676.904	3.119	PIMC_A3585
2.5087	8083831	92769.4	310.1	1283.561	3.902	PIMC_A3584
2.5087	16167663	187865.4	337.2	2484.609	4.243	PIMC_A3583
2.5087	32335325	378004.1	412.5	4880.292	5.206	PIMC_A3582
2.5087	64670651	756470.6	612.0	9644.225	7.704	PIMC_A3581
2.5087	129341301	1510913.9	833.1	19138.679	10.495	PIMC_A3580
2.5087	258682602	3024944.4	1072.2	38190.873	13.480	PIMC_A3579
2.5087	517365204	6054012.4	1131.2	76307.047	14.213	PIMC_A3578
5.0174	1347305	25101.2	503.4	200.936	3.166	PIMC_A3598
5.0174	2020958	38909.9	550.8	313.556	3.472	PIMC_A3597
5.0174	4041916	88884.2	486.5	655.812	3.062	PIMC_A3596
5.0174	8083831	185650.7	597.0	1276.586	3.755	PIMC_A3595
5.0174	16167663	374783.7	638.2	2472.912	4.010	PIMC_A3594
5.0174	32335325	753018.7	890.7	4856.619	5.603	PIMC_A3593
5.0174	64670651	1511237.5	1126.5	9629.535	7.068	PIMC_A3592
5.0174	129341301	3027710.6	1432.9	19172.825	8.963	PIMC_A3591
5.0174	258682602	6056069.4	2235.2	38226.650	14.063	PIMC_A3590
5.0174	517365204	12103991.4	2778.3	76278.717	17.526	PIMC_A3589
5.0175	6736	443.7	0.3	0.892	0.001	PBE_B4C120_0148
5.0175	10000	478.5	0.4	1.042	0.001	PBE_B4C120_0149
5.0175	20000	580.7	0.8	1.504	0.002	PBE_B4C120_0150
5.0175	50523	908.6	1.0	3.216	0.003	PBE_B4C120_0151
5.0175	67364	1106.9	1.1	4.344	0.004	PBE_B4C120_0152
5.0175	101047	1516.6	1.5	6.821	0.005	PBE_B4C120_0153
5.0175	126309	1838.0	0.9	8.832	0.003	PBE_B4C120_0154
5.0175	202095	2844.7	0.9	15.336	0.004	PBE_B4C120_0155
5.0175	252619	3535.9	2.1	19.938	0.008	PBE_B4C120_0156
5.0175	505239	7122.1	3.9	44.159	0.029	PBE_B4C30_0035
7.5261	1010479	24092.6	676.4	119.081	2.836	PIMC_A3610
7.5261	1347305	34984.9	616.5	180.443	2.586	PIMC_A3609
7.5261	2020958	58336.2	713.7	303.149	2.991	PIMC_A3608
7.5261	4041916	132474.5	725.5	643.917	3.038	PIMC_A3607
7.5261	8083831	278394.0	933.9	1270.287	3.920	PIMC_A3606
7.5261	16167663	561169.8	988.3	2464.149	4.144	PIMC_A3605
7.5261	32335325	1132212.6	1304.3	4864.353	5.483	PIMC_A3604
7.5261	64670651	2266120.7	1450.6	9624.077	6.105	PIMC_A3603
7.5261	129341301	4537038.6	2389.5	19151.236	9.991	PIMC_A3602
7.5261	258682602	9075883.8	3734.0	38189.980	15.688	PIMC_A3601
7.5261	517365204	18160616.9	3508.9	76296.115	14.737	PIMC_A3600
7.5262	6736	1336.5	0.5	1.866	0.001	PBE_B4C120_0158
7.5262	10000	1391.2	0.5	2.027	0.001	PBE_B4C120_0159
7.5262	20000	1545.6	0.8	2.501	0.001	PBE_B4C120_0160
7.5262	50523	2017.5	0.8	4.148	0.002	PBE_B4C120_0161
7.5262	67364	2297.1	1.4	5.208	0.003	PBE_B4C120_0162
7.5262	101047	2894.1	2.0	7.583	0.006	PBE_B4C120_0163
7.5262	126309	3372.8	2.5	9.535	0.007	PBE_B4C120_0164
7.5262	202095	4850.5	1.8	15.857	0.006	PBE_B4C120_0165
7.5262	252619	5870.5	1.9	20.376	0.006	PBE_B4C120_0166

continued ...

... continued

ρ (g/cm ³)	T (K)	P (GPa)	P_{error} (GPa)	E (Ha/B ₄ C)	E_{error} (Ha/B ₄ C)	note
7.5262	505239	11135.2	7.6	44.177	0.036	PBE_B4C30.0051
10.0349	6736	2699.3	0.6	3.105	0.001	PBE_B4C120.0168
10.0349	10000	2778.3	0.7	3.276	0.001	PBE_B4C120.0169
10.0349	20000	2989.2	1.1	3.770	0.002	PBE_B4C120.0170
10.0349	50523	3597.4	2.7	5.382	0.005	PBE_B4C120.0171
10.0349	67364	3954.4	3.0	6.403	0.006	PBE_B4C120.0172
10.0349	101047	4723.7	3.1	8.694	0.007	PBE_B4C120.0173
10.0349	126309	5332.8	2.9	10.572	0.006	PBE_B4C120.0174
10.0349	202095	7267.9	3.5	16.787	0.009	PBE_B4C120.0175
10.0349	252619	8592.0	4.0	21.239	0.010	PBE_B4C120.0176
10.0349	505239	15437.1	9.6	44.666	0.036	PBE_B4C30.0067
10.0349	1010479	34986.5	1044.5	123.038	3.285	PIMC_A3621
10.0349	1347305	46667.0	1012.2	173.850	3.185	PIMC_A3620
10.0349	2020958	77656.4	1082.6	294.180	3.405	PIMC_A3619
10.0349	4041916	177948.6	977.7	641.285	3.079	PIMC_A3618
10.0349	8083831	367611.3	1269.2	1254.130	3.992	PIMC_A3617
10.0349	16167663	746834.2	1262.5	2456.294	3.969	PIMC_A3616
10.0349	32335325	1508100.1	1689.9	4857.032	5.321	PIMC_A3615
10.0349	64670651	3023617.9	2169.2	9628.178	6.870	PIMC_A3614
10.0349	129341301	6043779.5	2638.7	19132.188	8.317	PIMC_A3613
10.0349	258682602	12096112.7	4951.6	38172.125	15.585	PIMC_A3612
10.0349	517365204	24216797.6	5382.9	76302.638	16.961	PIMC_A3611
11.2892	1010479	41709.7	1143.1	127.812	3.197	PIMC_A3632
11.2892	1347305	54706.0	1098.7	177.545	3.072	PIMC_A3631
11.2892	2020958	84970.2	1195.4	284.316	3.347	PIMC_A3630
11.2892	4041916	194649.0	1080.3	622.685	3.019	PIMC_A3629
11.2892	8083831	414955.6	1405.5	1255.831	3.931	PIMC_A3628
11.2892	16167663	838384.2	1474.3	2449.395	4.124	PIMC_A3627
11.2892	32335325	1692733.1	2027.9	4844.705	5.676	PIMC_A3626
11.2892	64670651	3407184.7	2353.1	9643.450	6.580	PIMC_A3625
11.2892	129341301	6802116.0	4041.0	19138.514	11.329	PIMC_A3624
11.2892	258682602	13620367.2	4405.1	38206.034	12.316	PIMC_A3623
11.2892	517365204	27241435.2	5301.2	76295.358	14.821	PIMC_A3622
12.5436	10000	4628.5	0.7	4.676	0.001	PBE_B4C120.0179
12.5436	20000	4901.3	1.2	5.196	0.002	PBE_B4C120.0180
12.5436	50523	5647.4	1.8	6.797	0.003	PBE_B4C120.0181
12.5436	67364	6070.7	1.0	7.780	0.002	PBE_B4C120.0182
12.5436	101047	6998.4	2.2	10.002	0.005	PBE_B4C120.0183
12.5436	126309	7737.4	5.0	11.839	0.010	PBE_B4C120.0184
12.5436	202095	10085.9	4.5	17.947	0.011	PBE_B4C120.0185
12.5436	252619	11697.0	4.5	22.338	0.011	PBE_B4C120.0186
12.5436	505239	20042.1	7.9	45.469	0.029	PBE_B4C30.0083
12.5436	1347305	58420.8	1183.6	169.416	2.978	PIMC_A3642
12.5436	2020958	98531.3	1292.6	291.848	3.249	PIMC_A3641
12.5436	4041916	216565.9	1198.0	620.836	3.019	PIMC_A3640
12.5436	8083831	457590.9	1556.2	1244.895	3.923	PIMC_A3639
12.5436	16167663	930693.5	1648.7	2445.848	4.151	PIMC_A3638
12.5436	32335325	1879207.6	2326.5	4839.516	5.857	PIMC_A3637
12.5436	64670651	3774359.1	3080.0	9613.114	7.730	PIMC_A3636
12.5436	129341301	7564430.1	3763.7	19153.993	9.483	PIMC_A3635
12.5436	258682602	15135191.9	5628.8	38208.688	14.165	PIMC_A3634
12.5436	517365204	30257769.9	4928.2	76268.123	12.396	PIMC_A3633
15.0523	1010479	53347.1	1465.9	117.897	3.077	PIMC_A3654
15.0523	1347305	73340.1	1428.0	171.417	2.997	PIMC_A3653
15.0523	2020958	119085.1	1610.1	288.524	3.371	PIMC_A3652
15.0523	4041916	262569.8	1486.4	621.390	3.115	PIMC_A3651
15.0523	8083831	552139.3	1882.7	1247.669	3.949	PIMC_A3650
15.0523	16167663	1117688.5	1965.7	2444.803	4.127	PIMC_A3649
15.0523	32335325	2260439.8	2810.9	4848.438	5.904	PIMC_A3648
15.0523	64670651	4537668.1	3241.8	9629.701	6.808	PIMC_A3647

continued ...

... continued

ρ (g/cm ³)	T (K)	P (GPa)	P_{error} (GPa)	E (Ha/B ₄ C)	E_{error} (Ha/B ₄ C)	note
15.0523	129341301	9069639.2	5110.8	19136.901	10.681	PIMC_A3646
15.0523	258682602	18144450.8	7854.1	38170.075	16.462	PIMC_A3645
15.0523	517365204	36320053.4	6770.2	76289.249	14.184	PIMC_A3644
15.0524	6736	6775.1	12.0	5.933	0.017	PBE_B4C120_0188
15.0524	20000	7261.8	1.1	6.704	0.001	PBE_B4C120_0190
15.0524	50523	8149.9	1.9	8.315	0.002	PBE_B4C120_0191
15.0524	67364	8648.5	2.2	9.287	0.004	PBE_B4C120_0192
15.0524	101047	9713.2	3.5	11.446	0.005	PBE_B4C120_0193
15.0524	126309	10560.4	3.8	13.222	0.007	PBE_B4C120_0194
15.0524	202095	13290.7	5.6	19.243	0.011	PBE_B4C120_0195
15.0524	252619	15162.4	6.5	23.602	0.016	PBE_B4C120_0196
15.0524	505239	24961.7	9.4	46.532	0.025	PBE_B4C30_0099
17.5610	1010479	62336.2	1580.2	115.857	2.836	PIMC_A3665
17.5610	1347305	85805.3	1608.8	168.247	2.891	PIMC_A3664
17.5610	2020958	136741.9	1818.2	279.581	3.273	PIMC_A3663
17.5610	4041916	300880.5	1708.3	607.206	3.071	PIMC_A3662
17.5610	8083831	641212.4	2159.3	1238.969	3.886	PIMC_A3661
17.5610	16167663	1305330.3	2254.3	2444.524	4.053	PIMC_A3660
17.5610	32335325	2628791.0	3092.4	4831.496	5.553	PIMC_A3659
17.5610	64670651	5290724.2	3841.7	9621.624	6.923	PIMC_A3658
17.5610	129341301	10568812.8	5871.5	19112.975	10.583	PIMC_A3657
17.5610	258682602	21175001.0	8164.4	38180.974	14.699	PIMC_A3656
17.5610	517365204	42363812.8	8271.6	76271.245	14.867	PIMC_A3655
17.5611	10000	9598.7	13.4	7.613	0.019	PBE_B4C120_0199
17.5611	20000	10070.4	1.8	8.279	0.002	PBE_B4C120_0200
17.5611	50523	11094.5	1.8	9.900	0.002	PBE_B4C120_0201
17.5611	67364	11661.7	2.9	10.860	0.004	PBE_B4C120_0202
17.5611	101047	12849.0	3.1	12.955	0.005	PBE_B4C120_0203
17.5611	126309	13818.2	4.7	14.720	0.007	PBE_B4C120_0204
17.5611	202095	16870.0	6.6	20.642	0.011	PBE_B4C120_0205
17.5611	252619	18989.2	6.6	24.999	0.016	PBE_B4C120_0206
17.5611	505239	30145.1	15.9	47.653	0.046	PBE_B4C30_0115
20.0697	1010479	70289.2	1815.5	111.781	2.854	PIMC_A3676
20.0697	1347305	93427.7	1819.3	158.288	2.859	PIMC_A3675
20.0697	2020958	159835.5	2151.1	281.486	3.384	PIMC_A3674
20.0697	4041916	341929.4	2005.1	599.969	3.152	PIMC_A3673
20.0697	8083831	725349.4	2370.9	1223.976	3.732	PIMC_A3672
20.0697	16167663	1489538.2	2722.7	2438.785	4.282	PIMC_A3671
20.0697	32335325	3008323.1	3484.4	4835.791	5.471	PIMC_A3670
20.0697	64670651	6033813.2	4696.1	9600.594	7.390	PIMC_A3669
20.0697	129341301	12085003.6	6140.8	19121.899	9.673	PIMC_A3668
20.0697	258682602	24204304.1	9811.3	38186.636	15.483	PIMC_A3667
20.0697	517365204	48408536.7	9345.6	76258.850	14.675	PIMC_A3666
20.0698	10000	12762.8	0.9	9.181	0.001	PBE_B4C120_0209
20.0698	20000	13320.4	1.4	9.905	0.001	PBE_B4C120_0210
20.0698	50523	14477.6	2.4	11.543	0.003	PBE_B4C120_0211
20.0698	67364	15100.8	4.8	12.485	0.006	PBE_B4C120_0212
20.0698	101047	16425.3	3.8	14.561	0.006	PBE_B4C120_0213
20.0698	126309	17466.7	4.6	16.264	0.008	PBE_B4C120_0214
20.0698	202095	20828.9	5.1	22.165	0.009	PBE_B4C120_0215
20.0698	252619	23147.8	6.6	26.468	0.013	PBE_B4C120_0216
20.0698	505239	35571.3	14.3	48.863	0.030	PBE_B4C30_0131
25.0872	1010479	87214.1	2216.6	107.373	2.787	PIMC_A3687
25.0872	1347305	123235.7	2239.0	160.989	2.820	PIMC_A3686
25.0872	2020958	196124.9	2664.1	269.727	3.354	PIMC_A3685
25.0872	4041916	428037.6	2444.2	593.804	3.077	PIMC_A3684
25.0872	8083831	908550.6	2946.7	1220.664	3.706	PIMC_A3683
25.0872	16167663	1864015.2	3317.5	2436.957	4.176	PIMC_A3682
25.0872	32335325	3747985.1	4716.4	4816.846	5.943	PIMC_A3681
25.0872	64670651	7543547.7	5674.7	9599.259	7.151	PIMC_A3680

continued ...

... continued

ρ (g/cm ³)	T (K)	P (GPa)	P_{error} (GPa)	E (Ha/B ₄ C)	E_{error} (Ha/B ₄ C)	note
25.0872	129341301	15119588.9	6727.7	19136.352	8.486	PIMC_A3679
25.0872	258682602	30258390.7	11453.7	38187.745	14.433	PIMC_A3678
25.0872	517365204	60534837.3	10922.3	76287.187	13.773	PIMC_A3677
30.1046	1010479	107601.8	2604.2	107.318	2.730	PIMC_A3698
30.1046	1347305	140893.9	2693.8	149.817	2.828	PIMC_A3697
30.1046	2020958	232091.0	3088.5	261.337	3.240	PIMC_A3696
30.1046	4041916	512012.4	2940.2	586.090	3.084	PIMC_A3695
30.1046	8083831	1078105.1	3821.0	1202.934	4.006	PIMC_A3694
30.1046	16167663	2228993.3	3817.0	2424.901	4.009	PIMC_A3693
30.1046	32335325	4520030.4	5136.8	4837.597	5.372	PIMC_A3692
30.1046	64670651	9058273.3	7317.4	9603.443	7.667	PIMC_A3691
30.1046	129341301	18123765.5	9637.7	19113.151	10.120	PIMC_A3690
30.1046	258682602	36320568.3	12420.2	38198.164	13.042	PIMC_A3689
30.1046	517365204	72622107.5	13340.5	76265.622	14.002	PIMC_A3688
37.6307	1010479	147119.9	3181.3	113.815	2.671	PIMC_A3709
37.6307	1347305	193405.1	3225.9	159.107	2.707	PIMC_A3708
37.6307	2020958	298300.7	3899.0	261.283	3.272	PIMC_A3707
37.6307	4041916	636287.4	3753.1	574.957	3.146	PIMC_A3706
37.6307	8083831	1348937.5	4607.3	1197.395	3.863	PIMC_A3705
37.6307	16167663	2777583.7	4929.8	2412.462	4.135	PIMC_A3704
37.6307	32335325	5640862.8	6172.6	4825.974	5.175	PIMC_A3703
37.6307	64670651	11304155.2	8029.8	9584.400	6.776	PIMC_A3702
37.6307	129341301	22665528.6	10246.9	19119.821	8.547	PIMC_A3701
37.6307	258682602	45377914.9	14656.3	38176.243	12.356	PIMC_A3700
37.6307	517365204	90789135.2	18077.2	76272.864	15.166	PIMC_A3699
50.1743	1010479	228810.2	3608.3	129.142	2.269	PIMC_A3379
50.1743	1347305	268222.6	3711.4	158.940	2.338	PIMC_A3378
50.1743	2020958	416612.9	4532.8	264.081	2.850	PIMC_A3377
50.1743	4041916	856514.5	3610.6	569.466	2.272	PIMC_A3376
50.1743	8083831	1808604.3	4427.3	1194.311	2.786	PIMC_A3375
50.1743	16167663	3717607.4	4748.5	2413.995	2.991	PIMC_A3374
50.1743	32335325	7494789.2	7111.9	4803.281	4.481	PIMC_A3373
50.1743	64670651	15097727.3	9275.7	9596.045	5.833	PIMC_A3372
50.1743	129341301	30227397.3	12043.7	19120.537	7.599	PIMC_A3371
50.1743	258682602	60498356.0	19034.1	38169.777	11.969	PIMC_A3370
50.1743	517365204	121037580.3	17009.5	76260.744	10.735	PIMC_A3369
2.5090	2000	9.3	0.8	0.231	0.001	PBE_ONCV_1.07
2.5090	6736	34.8	2.7	0.517	0.002	PBE_ONCV_1.07
2.5090	10000	59.7	3.9	0.658	0.004	PBE_ONCV_1.07
2.5090	35001	176.0	5.1	1.921	0.006	PBE_ONCV_1.07
2.5090	126313	714.1	8.2	8.732	0.018	PBE_ONCV_1.07
2.5090	673653	4948.3	34.5	78.542	0.149	PBE_ONCV_2.06
2.5090	842066	6686.7	22.2	111.475	0.101	PBE_ONCV_2.06
2.5090	1010479	8472.6	24.3	146.350	0.157	PBE_ONCV_2.06
2.5090	1347305	12374.3	15.2	214.048	0.098	PBE_ONCV_2.06
5.0170	6736	438.2	4.8	0.932	0.002	PBE_ONCV_1.07
5.0170	10000	488.2	6.3	1.113	0.004	PBE_ONCV_1.07
5.0170	35001	728.7	13.3	2.308	0.011	PBE_ONCV_1.07
5.0170	126313	1821.7	20.6	8.701	0.026	PBE_ONCV_1.07
5.0170	350013	4898.4	12.6	28.724	0.043	PBE_ONCV_2.06
5.0170	673653	9984.3	10.1	71.185	0.055	PBE_ONCV_2.06
5.0170	842066	12831.4	12.2	100.502	0.057	PBE_ONCV_2.06
5.0170	1010479	15990.7	33.0	130.330	0.106	PBE_ONCV_2.06
5.0170	1347305	23939.0	6.7	193.193	0.102	PBE_ONCV_2.06
7.5260	6736	1316.7	7.0	1.894	0.004	PBE_ONCV_1.07
7.5260	10000	1376.0	9.2	2.084	0.005	PBE_ONCV_1.07
7.5260	35001	1770.7	14.1	3.298	0.009	PBE_ONCV_1.07
7.5260	126313	3330.8	47.2	9.306	0.039	PBE_ONCV_1.07
7.5260	350013	7905.6	28.0	28.870	0.066	PBE_ONCV_2.06
7.5260	673653	15539.5	23.1	67.735	0.060	PBE_ONCV_2.06

continued ...

... continued

ρ (g/cm ³)	T (K)	P (GPa)	P_{error} (GPa)	E (Ha/B ₄ C)	E_{error} (Ha/B ₄ C)	note
7.5260	842066	20140.4	23.1	93.497	0.079	PBE_ONCV.2.06
7.5260	1010479	24590.6	16.9	119.636	0.104	PBE_ONCV.2.06
7.5260	1347305	34532.3	22.9	180.619	0.133	PBE_ONCV.2.06
10.0350	6736	2690.7	10.4	3.140	0.003	PBE_ONCV.1.07
10.0350	10000	2751.2	4.1	3.308	0.003	PBE_ONCV.1.07
10.0350	35001	3297.3	27.5	4.589	0.015	PBE_ONCV.1.07
10.0350	126313	5327.5	46.0	10.417	0.034	PBE_ONCV.1.07
10.0350	350013	11301.0	49.0	29.423	0.068	PBE_ONCV.2.06
10.0350	673653	21476.6	91.1	66.968	0.216	PBE_ONCV.2.06
10.0350	842066	27203.8	42.3	90.131	0.157	PBE_ONCV.2.06
10.0350	1010479	33457.0	74.1	117.018	0.187	PBE_ONCV.2.06
10.0350	1347305	46468.1	63.8	174.733	0.148	PBE_ONCV.2.06
11.2890	6736	3543.6	8.2	3.832	0.004	PBE_ONCV.1.07
11.2890	10000	3634.3	10.9	4.017	0.005	PBE_ONCV.1.07
11.2890	35001	4206.0	31.0	5.246	0.016	PBE_ONCV.1.07
11.2890	126313	6486.6	56.3	11.048	0.043	PBE_ONCV.1.07
11.2890	350013	13071.0	35.4	29.683	0.052	PBE_ONCV.2.06
11.2890	673653	24818.9	141.9	67.657	0.034	PBE_ONCV.2.06
11.2890	842066	30471.3	16.0	88.406	0.011	PBE_ONCV.2.06
11.2890	1010479	38382.2	67.2	116.519	0.023	PBE_ONCV.2.06
11.2890	1347305	52575.8	46.7	172.974	0.015	PBE_ONCV.2.06
12.5440	6736	4519.2	2.9	4.543	0.002	PBE_ONCV.2.06
12.5440	10000	4663.0	1.8	4.767	0.001	PBE_ONCV.2.06
12.5440	35001	5302.7	16.2	6.002	0.012	PBE_ONCV.2.06
12.5440	126313	7840.6	17.6	11.940	0.025	PBE_ONCV.2.06
12.5440	350013	15317.2	77.9	30.819	0.105	PBE_ONCV.2.06
12.5440	673653	26264.0	19.6	64.244	0.071	PBE_ONCV.2.06
12.5440	842066	34878.4	81.5	89.036	0.069	PBE_ONCV.2.06
12.5440	1010479	42918.5	22.6	115.451	0.023	PBE_ONCV.2.06
12.5440	1347305	58855.8	43.6	167.049	0.067	PBE_ONCV.2.06
15.0520	2000	6618.1	1.1	5.769	0.002	PBE_ONCV.2.06
15.0520	6736	6809.5	2.6	6.074	0.003	PBE_ONCV.2.06
15.0520	10000	6925.4	6.0	6.269	0.004	PBE_ONCV.2.06
15.0520	35001	7623.3	21.8	7.432	0.016	PBE_ONCV.2.06
15.0520	126313	10488.1	57.0	12.961	0.056	PBE_ONCV.2.06
15.0520	350013	19377.3	101.4	31.455	0.103	PBE_ONCV.2.06
15.0520	673653	33914.0	30.5	65.918	0.090	PBE_ONCV.2.06
15.0520	842066	41941.1	79.4	92.213	0.132	PBE_ONCV.2.06
15.0520	1010479	51904.3	97.5	113.040	0.125	PBE_ONCV.2.06
15.0520	1347305	72318.8	342.6	169.570	0.169	PBE_ONCV.2.06
17.5610	10000	9638.9	6.7	7.734	0.003	PBE_ONCV.2.06
17.5610	35001	10408.7	6.4	8.958	0.008	PBE_ONCV.2.06
17.5610	126313	13972.8	24.0	14.757	0.032	PBE_ONCV.2.06
17.5610	350013	24066.7	124.8	33.087	0.124	PBE_ONCV.2.06
17.5610	673653	40863.3	152.1	66.182	0.149	PBE_ONCV.2.06
17.5610	842066	50853.8	154.1	88.308	0.156	PBE_ONCV.2.06
17.5610	1010479	62119.5	333.4	116.191	0.141	PBE_ONCV.2.06
17.5610	1347305	84179.8	44.1	163.040	0.124	PBE_ONCV.2.06
20.0700	10000	12811.8	11.2	9.369	0.007	PBE_ONCV.2.06
20.0700	35001	13915.9	8.6	10.773	0.005	PBE_ONCV.2.06
20.0700	126313	17586.3	65.4	16.123	0.051	PBE_ONCV.2.06
20.0700	350013	28877.3	115.3	34.082	0.093	PBE_ONCV.2.06
20.0700	673653	48008.1	224.8	67.112	0.030	PBE_ONCV.2.06
20.0700	842066	59253.3	301.9	91.678	0.024	PBE_ONCV.2.06
20.0700	1010479	70396.8	89.0	111.236	0.066	PBE_ONCV.2.06
20.0700	1347305	97864.6	171.5	161.321	0.097	PBE_ONCV.2.06
25.0870	10000	20383.0	5.2	12.629	0.003	PBE_ONCV.2.06
25.0870	35001	21740.1	28.1	14.131	0.014	PBE_ONCV.2.06
25.0870	126313	26153.1	50.1	19.250	0.036	PBE_ONCV.2.06
25.0870	350013	40240.6	173.9	37.224	0.116	PBE_ONCV.2.06

continued ...

... continued

ρ (g/cm ³)	T (K)	P (GPa)	P_{error} (GPa)	E (Ha/B ₄ C)	E_{error} (Ha/B ₄ C)	note
25.0870	673653	62748.5	133.9	67.642	0.119	PBE_ONCV_2.06
25.0870	842066	76860.4	451.1	91.864	0.114	PBE_ONCV_2.06
25.0870	1010479	92273.8	551.9	110.436	0.141	PBE_ONCV_2.06
25.0870	1347305	124901.1	564.6	161.060	0.127	PBE_ONCV_2.06
30.1050	10000	29636.4	12.5	15.982	0.004	PBE_ONCV_2.06
30.1050	35001	31097.4	41.0	17.386	0.014	PBE_ONCV_2.06
30.1050	126313	36480.6	81.2	22.816	0.043	PBE_ONCV_2.06
30.1050	350013	52548.5	157.1	39.666	0.099	PBE_ONCV_2.06
30.1050	673653	79783.9	529.2	70.934	0.106	PBE_ONCV_2.06
30.1050	842066	98505.0	204.4	90.862	0.108	PBE_ONCV_2.06
30.1050	1010479	114099.0	653.8	113.600	0.100	PBE_ONCV_2.06
30.1050	1347305	151123.5	518.9	159.254	0.082	PBE_ONCV_2.06
37.6310	10000	46591.7	14.1	21.192	0.005	PBE_ONCV_2.06
37.6310	35001	48478.9	56.0	22.750	0.020	PBE_ONCV_2.06
37.6310	126313	54509.5	135.1	27.698	0.071	PBE_ONCV_2.06
37.6310	350013	74028.7	839.7	43.372	0.081	PBE_ONCV_2.06
37.6310	673653	108684.7	484.0	74.384	0.042	PBE_ONCV_2.06
37.6310	842066	127839.8	630.1	93.539	0.050	PBE_ONCV_2.06
37.6310	1010479	152358.0	600.1	113.126	0.070	PBE_ONCV_2.06
37.6310	1347305	200300.2	1428.8	160.424	0.047	PBE_ONCV_2.06
50.1750	10000	82106.4	25.8	29.732	0.008	PBE_ONCV_2.06
50.1750	35001	84498.8	67.5	31.221	0.026	PBE_ONCV_2.06
50.1750	126313	91888.0	151.8	35.933	0.055	PBE_ONCV_2.06
50.1750	350013	117311.6	756.2	59.691	0.298	PBE_ONCV_2.06
50.1750	673653	160348.0	612.3	83.482	0.161	PBE_ONCV_2.06
50.1750	842066	188902.7	1262.9	99.851	0.415	PBE_ONCV_2.06
50.1750	1010479	213986.7	1638.1	117.712	0.518	PBE_ONCV_2.06
50.1750	1347305	273743.7	1461.5	159.957	0.224	PBE_ONCV_2.06

* szha@lle.rochester.edu† marshall47@llnl.gov‡ militzer@berkeley.edu§ whitley3@llnl.gov¹ M. A. Barrios, D. G. Hicks, T. R. Boehly, D. E. Fratanduono, J. H. Eggert, P. M. Celliers, G. W. Collins, and D. D. Meyerhofer, *Phys. Plasmas* **17**, 056307 (2010).² M. A. Barrios, T. R. Boehly, D. G. Hicks, D. E. Fratanduono, J. H. Eggert, G. W. Collins, and D. D. Meyerhofer, *J. Appl. Phys.* **111**, 093515 (2012).³ T. Döppner, D. C. Swift, A. L. Kritcher, B. Bachmann, G. W. Collins, D. A. Chapman, J. Hawreliak, D. Kraus, J. Nilsen, S. Rothman, L. X. Benedict, E. Dewald, D. E. Fratanduono, J. A. Gaffney, S. H. Glenzer, S. Hamel, O. L. Landen, H. J. Lee, S. LePape, T. Ma, M. J. MacDonald, A. G. MacPhee, D. Milathianaki, M. Millot, P. Neumayer, P. A. Sterne, R. Tommasini, and R. W. Falcone, *Phys. Rev. Lett.* **121**, 025001 (2018).⁴ A. L. Kritcher, T. Döppner, D. Swift, J. Hawreliak, J. Nilsen, J. Hammer, B. Bachmann, G. Collins, O. Landen, C. Keane, S. Glenzer, S. Rothman, D. Chapman, D. Kraus, and R. Falcone, *J. Phys. Conf. Ser.* **688**, 012055 (2016).⁵ D. S. Clark, C. R. Weber, J. L. Milovich, J. D. Salmonson, A. L. Kritcher, S. W. Haan, B. A. Hammel, D. E. Hinkel, O. A. Hurricane, O. S. Jones, M. M. Marinak, P. K. Patel, H. F. Robey, S. M. Sepke, and M. J. Edwards, *Phys. Plasmas* **23**, 056302 (2016).⁶ S. Y. Gus'kov, N. N. Demchenko, N. V. Zmitrenko, D. V. Il'in, P. A. Kuchugov, V. B. Rozanov, V. E. Sherman, and R. A. Yakhin, *Journal of Russian Laser Research* **38**, 173 (2017).⁷ A. S. Moore, S. Prisbrey, K. L. Baker, P. M. Celliers, J. Fry, T. R. Dittrich, K.-J. J. Wu, M. L. Kervin, M. E. Schoff, M. Farrell, A. Nikroo, and O. A. Hurricane, *J. Phys. Conf. Ser.* **717**, 012038 (2016).⁸ R. E. Olson, G. A. Chandler, R. J. Leeper, A. Nobile, R. Wallace, J. A. Oertel, J. Faulkner, T. Archuletta, J. P. Knauer, R. E. Turner, K. Loughman, and V. Reki, "Indirect-drive inertial confinement fusion (icf) ablator characterization experiments at the omega laser facility," in *Current Trends in International Fusion Research – Proceedings of the Fourth Symposium*, edited by C. D. Orth and E. Panarella (NRC Research Press, National Research Council of Canada, Ottawa, 2007) pp. 241–247.⁹ A. J. MacKinnon, N. B. Meezan, J. S. Ross, S. Le Pape, L. Berzak Hopkins, L. Divol, D. Ho, J. Milovich, A. Pak, J. Ralph, T. Döppner, P. K. Patel, C. Thomas, R. Tommasini, S. Haan, A. G. MacPhee, J. McNaney, J. Caggiano, R. Hatarik, R. Bionta, T. Ma, B. Spears, J. R. Rygg, L. R. Benedetti, R. P. J. Town, D. K. Bradley, E. L. Dewald, D. Fittinghoff, O. S. Jones, H. R. Robey, J. D. Moody, S. Khan, D. A. Callahan, A. Hamza, J. Biener, P. M. Celliers, D. G. Braun, D. J. Erskine, S. T. Pris-

- brey, R. J. Wallace, B. Kozioziemski, R. Dylla-Spears, J. Sater, G. Collins, E. Storm, W. Hsing, O. Landen, J. L. Atherton, J. D. Lindl, M. J. Edwards, J. A. Frenje, M. Gatu-Johnson, C. K. Li, R. Petrasso, H. Rinderknecht, M. Rosenberg, F. H. Sguin, A. Zylstra, J. P. Knauer, G. Grim, N. Guler, F. Merrill, R. Olson, G. A. Kyrala, J. D. Kilkenny, A. Nikroo, K. Moreno, D. E. Hoover, C. Wild, and E. Werner, *Phys. Plasmas* **21**, 056318 (2014).
- ¹⁰ A. L. Kritcher, D. Clark, S. Haan, S. A. Yi, A. B. Zylstra, D. A. Callahan, D. E. Hinkel, L. F. Berzak Hopkins, O. A. Hurricane, O. L. Landen, S. A. MacLaren, N. B. Meezan, P. K. Patel, J. Ralph, C. A. Thomas, R. Town, and M. J. Edwards, *Phys. Plasmas* **25**, 056309 (2018).
- ¹¹ A. B. Zylstra, S. MacLaren, S. A. Yi, J. Kline, D. Callahan, O. Hurricane, B. Bachmann, G. Kyrala, L. Masse, P. Patel, J. E. Ralph, J. Salmonson, P. Volegov, and C. Wilde, *Phys. Plasmas* **26**, 052707 (2019).
- ¹² S. Zhang, B. Militzer, M. C. Gregor, K. Caspersen, L. H. Yang, J. Gaffney, T. Ogitsu, D. Swift, A. Lazicki, D. Erskine, R. A. London, P. M. Celliers, J. Nilsen, P. A. Sterne, and H. D. Whitley, *Phys. Rev. E* **98**, 023205 (2018).
- ¹³ A. C. Hayes, *Rep. Prog. Phys.* **80**, 026301 (2017).
- ¹⁴ R. Chen, Q. Shi, L. Su, M. Yang, Z. Huang, Y. Shi, Q. Zhang, Z. Liao, and T. Lu, *Ceramics International* **43**, 571 (2017).
- ¹⁵ S. Zhang, A. Lazicki, B. Militzer, L. H. Yang, K. Caspersen, J. A. Gaffney, M. W. Däne, J. E. Pask, W. R. Johnson, A. Sharma, P. Suryanarayana, D. D. Johnson, A. V. Smirnov, P. A. Sterne, D. Erskine, R. A. London, F. Coppari, D. Swift, J. Nilsen, A. J. Nelson, and H. D. Whitley, *Phys. Rev. B* **99**, 165103 (2019).
- ¹⁶ R. M. More, K. H. Warren, D. A. Young, and G. B. Zimmerman, *Phys. Fluids* **31**, 3059 (1988).
- ¹⁷ D. A. Young and E. M. Corey, *J. Appl. Phys.* **78**, 3748 (1995).
- ¹⁸ C. L. Ellison, H. D. Whitley, C. R. Brown, S. R. Copeland, W. J. Garbett, H. P. Le, M. B. Schneider, Z. B. Walters, H. Chen, J. I. Castor, R. S. Craxton, M. G. Johnson, E. M. Garcia, F. R. Graziani, G. E. Kemp, C. M. Krauland, P. W. McKenty, B. Lahmann, J. E. Pino, M. S. Rubery, H. A. Scott, R. Shepherd, and H. Sio, *Phys. Plasmas* **25**, 072710 (2018).
- ¹⁹ F. Thvenot, *Journal of the European Ceramic Society* **6**, 205 (1990).
- ²⁰ T. Fujii, Y. Mori, H. Hyodo, and K. Kimura, *J. Phys. Conf. Ser.* **215**, 012011 (2010).
- ²¹ P. Dera, M. H. Manghnani, A. Hushur, Y. Hu, and S. Tkachev, *Journal of Solid State Chemistry* **215**, 85 (2014).
- ²² M. Chen, J. W. McCauley, and K. J. Hemker, *Science* **299**, 1563 (2003).
- ²³ Y. Zhang, T. Mashimo, Y. Uemura, M. Uchino, M. Kodama, K. Shibata, K. Fukuoaka, M. Kikuchi, T. Kobayashi, and T. Sekine, *J. Appl. Phys.* **100**, 113536 (2006).
- ²⁴ T. J. Vogler, W. D. Reinhart, and L. C. Chhabildas, *J. Appl. Phys.* **95**, 4173 (2004).
- ²⁵ V. Domnich, Y. Gogotsi, M. Trenary, and T. Tanaka, *Applied Physics Letters* **81**, 3783 (2002).
- ²⁶ D. Ge, V. Domnich, T. Juliano, E. Stach, and Y. Gogotsi, *Acta Materialia* **52**, 3921 (2004).
- ²⁷ X. Q. Yan, W. J. Li, T. Goto, and M. W. Chen, *Applied Physics Letters* **88**, 131905 (2006).
- ²⁸ X. Q. Yan, Z. Tang, L. Zhang, J. J. Guo, C. Q. Jin, Y. Zhang, T. Goto, J. W. McCauley, and M. W. Chen, *Phys. Rev. Lett.* **102**, 075505 (2009).
- ²⁹ D. E. Grady, *J. Appl. Phys.* **117**, 165904 (2015).
- ³⁰ A. P. Awasthi and G. Subhash, *J. Appl. Phys.* **125**, 215901 (2019).
- ³¹ Q. An and W. A. Goddard, *Applied Physics Letters* **110**, 111902 (2017).
- ³² P. Korotaev, A. Kuksin, P. Pokatashkin, and A. Yanilkin, *AIP Conference Proceedings* **1793**, 070014 (2017).
- ³³ A. M. Molodets, A. A. Golyshev, and D. V. Shakhrai, *Journal of Experimental and Theoretical Physics* **124**, 469 (2017).
- ³⁴ A. Jay, O. Hardouin Duparc, J. Sjakste, and N. Vast, *J. Appl. Phys.* **125**, 185902 (2019).
- ³⁵ D. E. Fratanduono, P. M. Celliers, D. G. Braun, P. A. Sterne, S. Hamel, A. Shamp, E. Zurek, K. J. Wu, A. E. Lazicki, M. Millot, and G. W. Collins, *Phys. Rev. B* **94**, 184107 (2016).
- ³⁶ A. Shamp, E. Zurek, T. Ogitsu, D. E. Fratanduono, and S. Hamel, *Phys. Rev. B* (2017), 10.1103/PhysRevB.95.184111.
- ³⁷ B. Wilson, V. Sonnad, P. Sterne, and W. Isaacs, *J. Quant. Spectrosc. Radiat. Transfer* **99**, 658 (2006).
- ³⁸ B. Militzer, Ph.D. Thesis, University of Illinois at Urbana-Champaign (2000).
- ³⁹ D. M. Ceperley, *Rev. Mod. Phys.* **67**, 279 (1995).
- ⁴⁰ C. Pierleoni, D. M. Ceperley, B. Bernu, and W. R. Magro, *Phys. Rev. Lett.* **73**, 2145 (1994).
- ⁴¹ K. P. Driver and B. Militzer, *Phys. Rev. Lett.* **108**, 115502 (2012).
- ⁴² V. Natoli and D. M. Ceperley, *J. Comp. Phys.* **117**, 171 (1995).
- ⁴³ B. Militzer, *Comput. Phys. Commun.* **204**, 88 (2016).
- ⁴⁴ H. K. Clark and J. L. Hoard, *Journal of the American Chemical Society* **65**, 2115 (1943).
- ⁴⁵ S. Zhang, K. P. Driver, F. Soubiran, and B. Militzer, *Phys. Rev. E* **96**, 013204 (2017).
- ⁴⁶ S. Zhang, B. Militzer, L. X. Benedict, F. Soubiran, P. A. Sterne, and K. P. Driver, *J. Chem. Phys.* **148**, 102318 (2018).
- ⁴⁷ By comparing the EOS and the radial distribution function $g(r)$ obtained using 30-atom cells to those using 120-atom cells in our DFT-MD calculations, we find negligible differences at temperatures above 5×10^4 K. A comparison in $g(r)$ is shown in Fig. 9.
- ⁴⁸ P. E. Blöchl, O. Jepsen, and O. K. Andersen, *Phys. Rev. B* **49**, 16223 (1994).
- ⁴⁹ D. R. Hamann, *Phys. Rev. B* **88**, 085117 (2013).
- ⁵⁰ D. R. Hamann, *Phys. Rev. B* **95**, 239906 (2017).
- ⁵¹ S. Goedecker, *Rev. Mod. Phys.* **71**, 1085 (1999).
- ⁵² D. R. Bowler and T. Miyazaki, *Rep. Progr. Phys.* **75**, 036503 (2012).
- ⁵³ G. Kresse and J. Furthmüller, *Phys. Rev. B* **54**, 11169 (1996).
- ⁵⁴ J. P. Perdew, K. Burke, and M. Ernzerhof, *Phys. Rev. Lett.* **77**, 3865 (1996).
- ⁵⁵ L. H. Yang, R. Q. Hood, J. E. Pask, and J. E. Klepeis, *J. Comput.-Aided Mater. Des.* **14**, 337 (2007).
- ⁵⁶ S. Nosé, *J. Chem. Phys.* **81**, 511 (1984).
- ⁵⁷ B. Militzer, *Phys. Rev. B* **79**, 155105 (2009).
- ⁵⁸ K. P. Driver and B. Militzer, *Phys. Rev. B* **93**, 064101 (2016).
- ⁵⁹ K. P. Driver, F. Soubiran, S. Zhang, and B. Militzer, *J. Chem. Phys.* **143**, 164507 (2015).

- ⁶⁰ S. Zhang, K. P. Driver, F. Soubiran, and B. Militzer, *High Energ. Dens. Phys.* **21**, 16 (2016).
- ⁶¹ S. Zhang, K. P. Driver, F. Soubiran, and B. Militzer, *J. Chem. Phys.* **146**, 074505 (2017).
- ⁶² K. P. Driver, F. Soubiran, and B. Militzer, *Phys. Rev. E* **97**, 063207 (2018).
- ⁶³ B. Militzer and K. P. Driver, *Phys. Rev. Lett.* **115**, 176403 (2015).
- ⁶⁴ K. P. Driver and B. Militzer, *Phys. Rev. E* **95**, 043205 (2017).
- ⁶⁵ F. Soubiran, F. González-Cataldo, K. P. Driver, S. Zhang, and B. Militzer, *J. Chem. Phys.* **151**, 214104 (2019).
- ⁶⁶ F. González-Cataldo, F. Soubiran, H. Peterson, and B. Militzer, *Phys. Rev. B* **101**, 1 (2020).
- ⁶⁷ F. J. Rogers and H. E. DeWitt, *Phys. Rev. A* **8**, 1061 (1973).
- ⁶⁸ F. J. Rogers, *Phys. Rev. A* **10**, 2441 (1974).
- ⁶⁹ F. J. Rogers, *Phys. Rev. A* **19**, 375 (1979).
- ⁷⁰ F. J. Rogers, *Phys. Rev. A* **24**, 1531 (1981).
- ⁷¹ D. Johnson, A. Smirnov, and S. Khan, *MECCA: Multiple-scattering Electronic-structure Calculations for Complex Alloys (KKR-CPA Program, ver. 2.0)* (Iowa State University and Ames Laboratory, Ames, 2015).
- ⁷² S. H. Vosko, L. Wilk, and M. Nusair, *Canadian Journal of Physics* **58**, 1200 (1980), <https://doi.org/10.1139/p80-159>.
- ⁷³ H. J. Monkhorst and J. D. Pack, *Phys. Rev. B* **13**, 5188 (1976).
- ⁷⁴ E. I. Moses, R. N. Boyd, B. A. Remington, C. J. Keane, and R. Al-Ayat, *Phys. Plasmas* **16**, 041006 (2009).
- ⁷⁵ P. M. Celliers, D. K. Bradley, G. W. Collins, D. G. Hicks, T. R. Boehly, and W. J. Armstrong, *Rev. Sci. Instrum.* **75**, 4916 (2004).
- ⁷⁶ D. E. Fratanduono, D. H. Munro, P. M. Celliers, and G. W. Collins, *J. Appl. Phys.* **116**, 033517 (2014).
- ⁷⁷ L. X. Benedict, K. P. Driver, S. Hamel, B. Militzer, T. Qi, A. A. Correa, A. Saul, and E. Schwegler, *Phys. Rev. B* **89**, 224109 (2014).
- ⁷⁸ M. C. Marshall, A. E. Lazicki, D. Erskine, R. A. London, D. E. Fratanduono, P. M. Celliers, J. H. Eggert, F. Coppari, D. C. Swift, P. A. Sterne, H. D. Whitley, and J. Nilsen, *Phys. Rev. B* **99**, 174101 (2019).
- ⁷⁹ A. Jenei, A. Kritcher, D. Swift, et al., *private communication*.
- ⁸⁰ J. A. Gaffney, S. T. Brandon, K. D. Humbird, M. K. G. Kruse, R. C. Nora, J. L. Peterson, and B. K. Spears, *Phys. Plasmas* **26**, 082704 (2019).
- ⁸¹ H. D. Whitley, G. E. Kemp, C. Yeamans, Z. Walters, B. E. Blue, W. Garbett, M. Schneider, R. S. Craxton, E. M. Garcia, P. W. McKenty, M. Gatu-Johnson, K. Caspersen, J. I. Castor, M. Dne, C. L. Ellison, J. Gaffney, F. R. Graziani, J. Klepeis, N. Kostinski, A. Kritcher, B. Lahmann, A. E. Lazicki, H. P. Le, R. A. London, B. Maddox, M. Marshall, M. E. Martin, B. Militzer, A. Nikroo, J. Nilsen, T. Ogitsu, J. Pask, J. E. Pino, M. Rubery, R. Shepherd, P. A. Sterne, D. C. Swift, L. Yang, and S. Zhang, “Comparison of ablaters for the polar direct drive exploding pusher platform,” (2020), [arXiv:2006.15635 \[physics.comp-ph\]](https://arxiv.org/abs/2006.15635).
- ⁸² C. Yeamans, G. Kemp, Z. Walters, H. Whitley, P. McKenty, E. Garcia, Y. Yang, R. Craxton, and B. E. Blue, “High yield polar direct drive fusion neutron sources at the national ignition facility,” (2020), submitted.
- ⁸³ M. P. Allen and D. J. Tildesley, *Computer Simulation of Liquids* (Oxford Science Publications, 1987).
- ⁸⁴ The 5-atom structure has four B forming a face-centered cubic lattice and one C at the body center of the cell; the 10-atom structure consists of two C forming a body-centered cubic lattice that interconnects with 8 B that occupy the $(\pm 1/4, \pm 1/4, \pm 1/4)$ and $(\pm 3/4, \pm 3/4, \pm 3/4)$ sites and form a simple-cubic lattice; the 15-atom structure is a pseudo-rhombohedral phase of B₄C consisting of a boron icosahedra and a carbon chain.
- ⁸⁵ D. Swift, J. Hawreliak, D. Braun, A. Kritcher, S. Glenzer, G. W. Collins, S. Rothman, D. Chapman, and S. Rose, *AIP Conf. Proc.* **1426**, 477 (2012).
- ⁸⁶ J. Nilsen, B. Bachmann, G. Zimmerman, R. Hatarik, T. Döppner, D. Swift, J. Hawreliak, G. Collins, R. Falcone, S. Glenzer, *et al.*, *High Energ. Dens. Phys.* **21**, 20 (2016).
- ⁸⁷ D. C. Swift, A. L. Kritcher, J. A. Hawreliak, A. Lazicki, A. MacPhee, B. Bachmann, T. Döppner, J. Nilsen, G. W. Collins, S. Glenzer, S. D. Rothman, D. Kraus, and R. W. Falcone, *Rev. Sci. Instrum.* **89**, 053505 (2018).
- ⁸⁸ T. Döppner, D. Swift, A. Kritcher, B. Bachmann, G. Collins, D. Chapman, J. Hawreliak, D. Kraus, J. Nilsen, S. Rothman, L. Benedict, E. Dewald, D. Fratanduono, J. Gaffney, S. Glenzer, S. Hamel, O. Landen, H. Lee, S. LePape, T. Ma, M. MacDonald, A. MacPhee, D. Milathianaki, M. Millot, P. Neumayer, P. Sterne, R. Tomasini, and R. Falcone, *Phys. Rev. Lett.* **121**, 025001 (2018).